Bulletin of Volcanology (2018) 80: 83
https://doi.org/10.1007/s00445-018-1252-y

RESEARCH ARTICLE

Dynamics of shallow hydrothermal eruptions: new insights from Vulcano's Breccia di Commenda eruption

Mauro Rosi[1] · Federico Di Traglia[2] · Marco Pistolesi[1] · Tomaso Esposti Ongaro[3] · Mattia de' Michieli Vitturi[3] · Costanza Bonadonna[4]

Received: 1 February 2018 / Accepted: 29 September 2018 / Published online: 8 November 2018

Abstract

Understanding the dynamics and effects of hydrothermal eruptions is crucial to the hazard assessment in both volcanic and geothermal areas. Eruptions from hydrothermal centres may occur associated with magmatic phases, but also as isolated events without magmatic input, with the most recent examples being those of Te Maari (Tongariro, New Zealand) in 2012 and Ontake (Japan) in 2014. The most recent caldera of the Island of Vulcano (southern Italy) hosts in its centre the La Fossa cone, active since 5.5 ka and now characterised by continuous fumarolic degassing. In historical times, La Fossa cone has experienced several hydrothermal eruptions, with the most violent event being the Breccia di Commenda eruption that occurred during the thirteenth century AD. Based on analysis of 170 stratigraphic logs, we show that the Breccia di Commenda eruption occurred in three main phases. After an opening, low-intensity ash emission phase (phase 1), the eruption energy climaxed during phase 2, when a series of violent explosions produced an asymmetric shower of ballistic blocks and the contemporaneous emplacement of highly dispersed, lithic-rich, blast-like pyroclastic density currents (PDCs). The tephra units emplaced during phase 2, ranging in volume from 0.2 to 2.7×10^5 m^3, were covered in turn by thin ash fall deposits (phase 3). The dynamics of the most violent and intense stage of the eruption (phase 2) was investigated by numerical simulations. A three-dimensional numerical model was applied, describing the eruptive mixture as a Eulerian–Eulerian, two-phase, non-equilibrium gas-particle fluid (plus a one-way coupled Lagrangian ballistic block fraction). At the initial simulation time, a mass of about 10^9 kg, with initial overpressure above 10 MPa, and a temperature of 250 °C, was suddenly ejected from a 200-m-long, eastward inclined, NNE–SSW trending fissure. The mass release formed blast-like PDCs on both sides of the fissure and launched ballistic blocks eastwards. Field investigations and numerical simulations confirm that hydrothermal explosions at La Fossa cone include intense ballistic fallout of blocks, emission of PDCs potentially travelling beyond the La Fossa caldera and significant ash fallout. The hazard associated with both ballistic impact and PDC ingress, as associated with hydrothermal eruption, is significantly larger with respect to that associated with Vulcanian-type events of La Fossa.

Keywords Hydrothermal eruption dynamics · Pyroclastic density currents hazard · Volcano ballistic hazard · 3D numerical modelling · Island of Vulcano

Editorial responsibility: P-S. Ross

Electronic supplementary material The online version of this article (https://doi.org/10.1007/s00445-018-1252-y) contains supplementary material, which is available to authorized users.

✉ Federico Di Traglia
federico.ditraglia@unifi.it

[1] Dipartimento di Scienze della Terra, Università di Pisa, Via Santa Maria 53, 56126 Pisa, Italy

[2] Dipartimento di Scienze della Terra, Università degli Studi di Firenze, Via La Pira 4, 50121 Florence, Italy

[3] Istituto Nazionale di Geofisica e Vulcanologia, Sezione di Pisa, Via della Faggiola 32, 56126 Pisa, Italy

[4] Département des Sciences de la Terre, Université de Genève, Rue des Maraîchers 13, CH-1205 Geneva, Switzerland

Introduction and rationale for the study

Phreatic eruptions result when heated groundwater is the driving fluid (Barberi et al. 1992; Germanovich and Lowell 1995; Strehlow et al. 2017), and hydrothermal events occur when fluids from a pre-existing hydrothermal system are thought to be involved (Marini et al. 1993; Mastin 1995; Browne and Lawless 2001). Such eruptions are typically lithic-rich, and understanding their dynamics is crucial in assessing hazard in active volcanic and geothermal areas (Montalto 1995; Stix and de Moor 2018). These eruptions may occur as isolated events (Le Guern 1980; Sheridan 1980; Marini et al. 1993; Yamamoto et al. 1999; Ohba et al. 2007; Fujinawa et al. 2008; Houghton et al. 2011; Miura et al. 2012; Montanaro et al. 2016a,b; Mannen et al. 2018) or may be associated with magmatic phases (Chrétien and Brousse 1989; Calvache and Williams 1992; Gardner and White 2002). In the latter case, there may be precursory activity, on the former there may not (Barberi et al. 1992; Strehlow et al. 2017). Recent events of the isolated (phreatic event at a hydrothermal system) category have occurred at Te Maari craters (Tongariro volcanic complex, New Zealand) in August 2012 (Lube et al. 2014) and at Ontake volcano (Japan) in September 2014 (Oikawa et al. 2016). During the Ontake event, 64 climbers lost their lives (Tsunematsu et al. 2016), demonstrating the potential hazard presented by this type of volcanic phenomenon which involves a sudden explosion with little (to no) warning. Worldwide, active volcanoes in a quiescent state often attract large numbers of tourists crowding active degassing areas overlying very active hydrothermal systems (Heggie 2009; Erfurt-Cooper 2011). Phreatic/hydrothermal explosive events can occur with little or no precursors (e.g. Chrétien and Brousse 1989; Hurst et al. 2014; Kato et al. 2016) and can generate lethal phenomena such as intense showers of blocks and highly energetic pyroclastic density currents (PDCs; e.g. Sheridan and Malin 1983; Fitzgerald et al. 2014; Tanaka et al. 2018). Volcanologists, therefore, need to understand better the processes that drive their occurrence and to accurately assess their hazards (e.g. Barberi et al. 1992; Hincks et al. 2014; Fitzgerald et al. 2017).

The Island of Vulcano (Aeolian Archipelago), located in southern Italy (Fig. 1), hosts in its northern part a caldera (Gioncada and Sbrana 1991; Ventura 1994, Ventura et al. 1999; Ruch et al. 2016). Activity has been concentrated in the last 5000 years at La Fossa cone and at Vulcanello peninsula (Frazzetta et al. 1984; De Astis et al. 2013; Fusillo et al. 2015). The La Fossa caldera is characterised by large-scale degassing phenomena, most of which occurs through high-temperature fumaroles within the summit crater of the cone (occasionally up to more than 600 °C; Chiodini et al. 1995; Granieri et al. 2006; Diliberto 2017) and as widespread soil degassing within the crater and on its flanks which feeds boiling mud pools and underwater degassing manifestations around the harbour area (Chiodini et al. 1996; Capasso et al. 1997; Harris and Stevenson 1997; Federico et al. 2010; Paonita et al. 2013; Capasso et al. 2014; Mandarano et al. 2016). During the summer season, the island hosts up to 20,000 people, with hundreds of tourists climbing every day following marked and maintained trails into the Fossa crater (Biass et al. 2016a). Because La Fossa cone experienced a lithic-rich eruption (the Breccia di Commenda event) during the thirteenth century AD (Gurioli et al. 2012), and other similar events likely occurred in 1444 and in 1727 AD from vents opening on the northern flank and at the summit of the cone (Mercalli and Silvestri 1891; De Fiore 1922; Frazzetta et al. 1983; Di Traglia et al. 2013), the study of these events is particularly relevant for risk assessment and crisis management in a highly visited and populated volcanic setting.

The present study thus follows up on that of Gurioli et al. (2012) in its aim to more fully understand the physical and sedimentological processes that occurred during the Breccia di Commenda event. This is achieved through the integration of detailed field and laboratory analyses of deposits, as well as numerical modelling of PDCs and ballistic blocks dispersal of the most energetic phase during the eruption. Assessment of the physical volcanology of the Breccia di Commenda event, and a comparison with similar events that occurred at volcanoes with active hydrothermal systems (e.g. Sheridan 1980; Lube et al. 2014; Oikawa et al. 2016) also highlights similarities in terms of timing, eruptive mechanisms and energy release between geographically diverse, but process-similar, systems across the globe.

Geological and volcanological background

The Island of Vulcano consists of six volcanic edifices whose formation overlapped in time and space beginning 120 ka (Keller 1980; De Astis et al. 2013). The northern part of the island (Fig. 1) hosts a 4 × 2 km caldera structure (La Fossa Caldera; Gioncada and Sbrana 1991; Ventura 1994, Ventura et al. 1999; Romagnoli et al. 2012; Ruch et al. 2016) whose borders are exposed in the southern and western sectors. In historical times, volcanic activity has occurred at two centres within the caldera: at La Fossa cone that began to erupt 5.5 ka and which is located almost in the centre of the caldera (Frazzetta et al. 1984; De Astis et al. 2013) (Fig. 1), and at the Vulcanello islets, located along the northernmost border of the caldera. The Vulcanello vent was likely active both in Roman time (Mercalli and Silvestri 1891; De Fiore 1922) and between the eleventh and seventeenth centuries AD (Arrighi et al. 2006; Davì et al. 2009a; Fusillo et al. 2015). Magmatic eruptions at Vulcano Island are related to the ascent of deep basic (basaltic/shoshonitic) magmas that trigger episodes of recharge and mixing towards the upper magmatic reservoirs (Nicotra et al. 2018). The recent eruptive activity (< 2 ka) appears to have

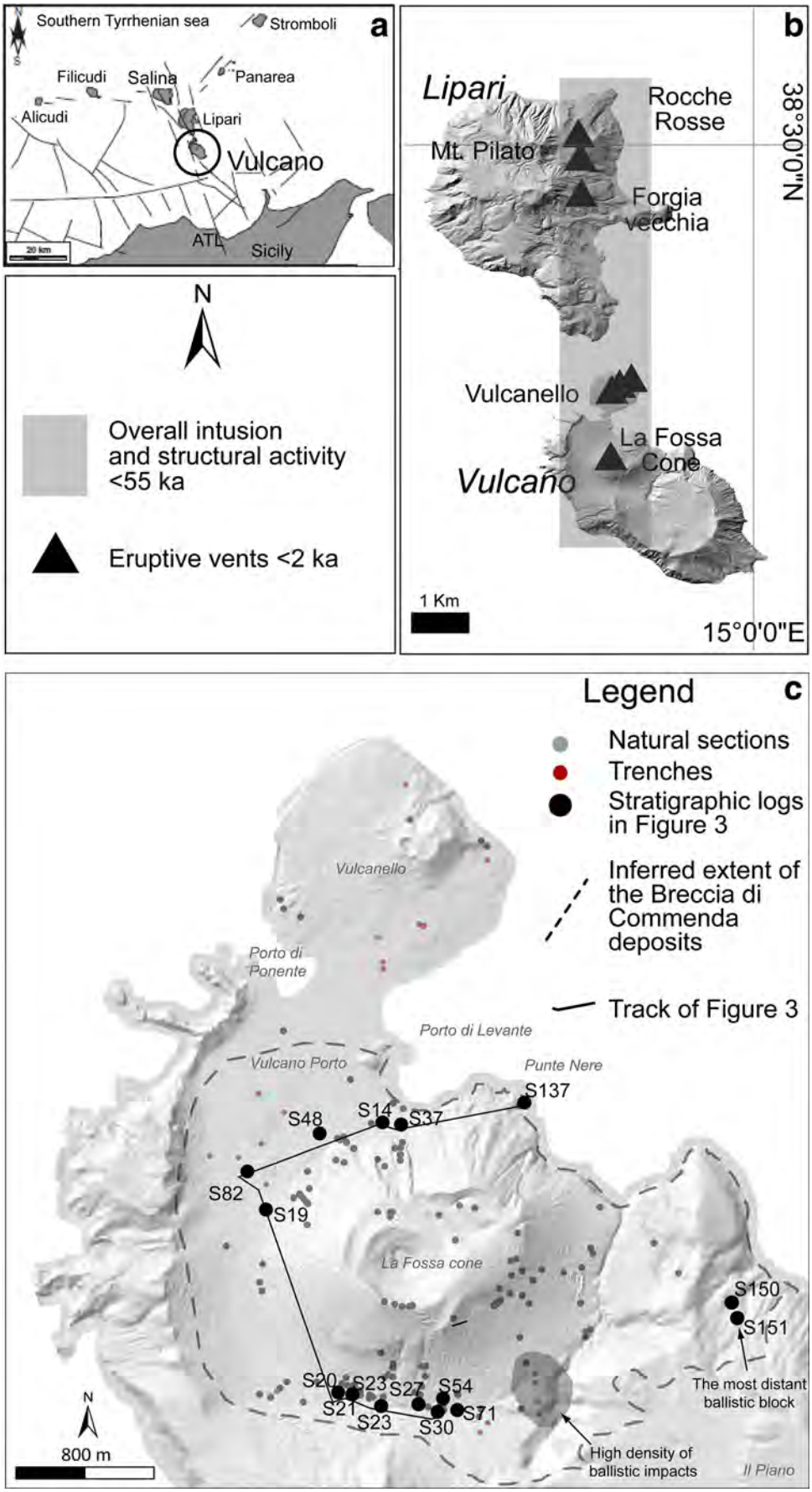

Fig. 1 **a** Geographic location and tectonic background of the Aeolian Archipelago. **b** Digital Elevation Model (DEM) of the Lipari and Vulcano islands, highlighting the location of the recent (< 55 ka) eruptive and tectonic activity (following Ruch et al. 2016). The location of the < 2 ka eruptive vents are also reported. **c** Map of the northern part of the Island of Vulcano. Main geographic features, location of the analysed stratigraphic natural sections and trenches are reported, with the inferred extent of the BdC deposits

been also controlled by the activity of the N–S trending, regional fault (Ventura 1994, Ventura et al. 1999; Ruch et al. 2016).

The Breccia di Commenda eruption

Several previous studies have addressed the Breccia di Commenda deposits, which was referred to as the Breccia di Commenda in Gurioli et al. (2012), as Commenda Eruptive Unit in Di Traglia et al. (2013) or as Caruggi formation in Dellino et al. (2011), De Astis et al. (2006) and De Astis et al. (2013). Frazzetta et al. (1983) described the Breccia di Commenda (namely 'Marker bed Explosion Breccia (EB)') as a phreatic explosive breccia composed of yellow fragments (due to fumarolic alteration) and ranging in composition from trachyte to andesite. Frazzetta et al. (1983) also described the unit as being roughly separated into an ash fall sub-unit scattered around the crater and a coarse-grained flow sub-unit cropping out near the base of the cone. According to Dellino et al. (2011) and De Astis et al. (2013), this 'Caruggi formation' was emplaced around 1250 years BP and mainly consists of lithic clasts characterised by a high degree of hydrothermal alteration. From deposit base to top, Dellino et al. (2011) and De Astis et al. (2013) recognised an exotic fine ash layer related to the eruption of Mt. Pilato that occurred in the neighbouring Island of Lipari, a metre-thick layer of dense lapilli and blocks set in an ash matrix, a dense lapilli- and blocks-bearing layer and a final, thinly laminated ash layer. According to Di Traglia et al. (2013), the Breccia di Commenda eruption was part of the Palizzi–Commenda Eruptive Cluster, which precedes the last eruptive cycle at La Fossa (Gran Cratere eruptive cluster; 1444–1890 AD; Fig. 2a).

The Palizzi–Commenda eruptive cluster can, in fact, be divided to a younger unit (Palizzi eruptive unit; 1170 ± 20 AD to 1230 ± 20 AD) followed by the Commenda eruptive unit (Di Traglia et al. 2013). This consists of a lower breccia deposit (Breccia di Commenda, Gurioli et al. 2012; the focus of this study), overlain by a sequence of thinly stratified reddish ash layers (varicoloured tuffs or 'Tufi Varicolori'—in Italian; Frazzetta et al. 1983; Capaccioni and Coniglio 1995; Dellino et al. 2011; Fig. 2a). Despite the variability of the nomenclature used in the recent literature to designate the deposits of this event, for the sake of simplicity we have adopted the term 'Breccia di Commenda' (hereafter BdC) eruption to refer to the coarse-grained, breccia sequence, and 'Tufi Varicolori' to refer to the fine ash sequence on top of it.

A relevant feature of the BdC event is represented by its contemporaneity with the explosive eruption of the Rocche Rosse (Cortese et al. 1986; Dellino and La Volpe 1995; Forni et al. 2013), whose vent was located on the Island of Lipari, within the Monte Pilato cone, about 12 km north of the La Fossa crater. The Rocche Rosse eruption was characterised by a first phase of explosive activity (Forni et al. 2013) which culminated with the emplacement of the Rocche Rosse lava flow (Bullock et al. 2018) dated at 1230 ± 20 AD (Arrighi et al. 2006; Fig. 2a). White, fine-grained ash layers with a rhyolite composition (Rocche Rosse tephra; Cortese et al. 1986) are in fact ubiquitously interbedded with the BdC deposits (Gurioli et al. 2012; Di Traglia et al. 2013; Fig. 2b).

Both in our reconstruction and in the work of Gurioli et al. (2012) (Table 1), 'phase' refers to a stage of the eruption characterised by certain dynamics, whereas 'layer' indicates the deposit associated with this phase. Following the reconstruction of Gurioli et al. (2012), during the BdC eruption, 2×10^6 m^3 of lithic-rich deposits were emplaced mainly as PDCs and minor fallout. The material ejected during the initial phase of the eruption (phase 1) consisted of grey-coloured, altered lithic ash, which was dispersed by a convective plume towards the NW, producing a few millimetre-thick ash bed rich in millimetre-size ash pellets (layer 1). Phase 1 thus represents the opening phase of the BdC eruption and shortly preceded the deposition on the Island of Vulcano of the first Rocche Rosse rhyolite ash-fall bed (Gurioli et al. 2012). Following the deposition of the Rocche Rosse tephra, the eruption energy suddenly escalated at La Fossa to produce phase 2. This phase produced a shower of ballistic blocks and the emplacement of lithic-rich, dilute PDC deposits (to form layers 2a and 2b) mostly towards the S and SE sectors, followed by the emission of a topographically controlled, coarse-grained, dense PDC (layer 2c). According to rock magnetic measurements, phase 2 deposits had a deposition temperature of 200–260 °C, consistent with their heating by the hydrothermal system present in the La Fossa cone edifice before the BdC eruption (Fulignati et al. 1998; Gurioli et al. 2012). Phase 2 was closed by the emplacement of layer 2d, whose deposits consist of 5–10-cm-thick lenses of brown-yellow, massive, well-sorted coarse ash (Gurioli et al. 2012). The eruption ended with a long-lasting emission of ash and with the emplacement of 'wet' ash fall deposits (phase 3), in which non-structured accretionary lapilli are often preserved.

According to Gurioli et al. (2012), the presence of non-vesicular juvenile fragments (20 to 40% by volume) in the deposits, varying in composition from rhyolite to trachyandesite, can be interpreted as indicative of the involvement of juvenile magma. This interacted during its ascent with the hydrothermal system to trigger a magmatic–hydrothermal eruption. The fine ash fraction, which is generally scarce in all BdC deposits, is also richer in S, Cu, Zn, Pb and As than the juvenile components of other La Fossa cone units, suggesting that the BdC eruption involved an interaction with a hydrothermal system anomalously enriched in S and metals (Fulignati et al. 1998).

Activity at La Fossa before the Breccia di Commenda eruption

The large amount of lithics which characterises the BdC eruption can be related to the material emplaced during previous

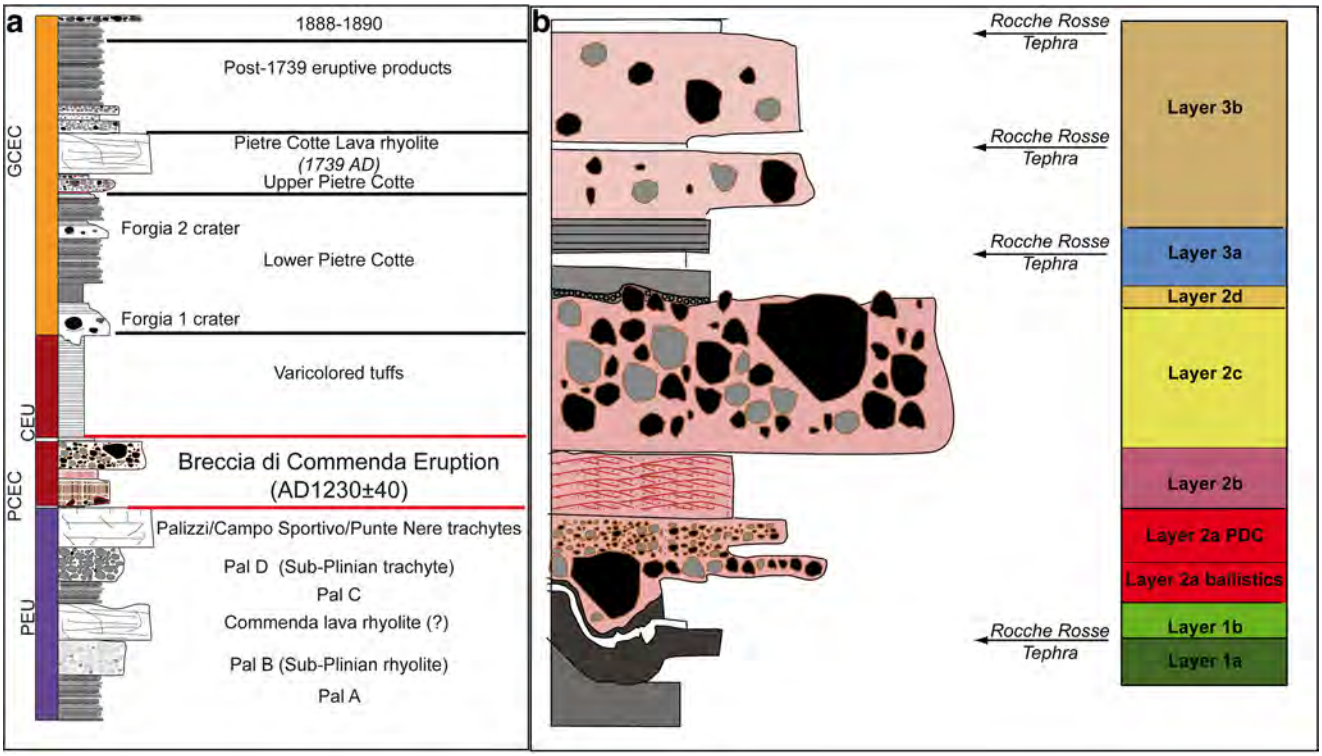

Fig. 2 **a** Synthetic log of the deposits related to the last 1000 years of eruptive activity at the La Fossa cone, modified after Di Traglia et al. (2013). The stratigraphic position of the Commenda lava is uncertain, and considered older (De Astis et al. 2013) or younger (Di Traglia et al. 2013) than the Palizzi/Campo Sportivo trachytic lavas. **b** Detailed stratigraphy of the deposits related to the Breccia di Commenda eruption. Labels for the different layers are explained in the main text. PCEC, Palizzi-Commenda Eruptive Cluster; PEU, Palizzi Eruptive Unit; CEU, Commenda Eruptive Unit; GCEC, Gran Cratere Eruptive Cluster

eruptive events. We thus briefly summarise below pre-BdC activity at La Fossa, based on available literature reconstructions (Fig. 2a). A re-examination of the volcanic evolution of the La Fossa cone between the twelfth and thirteenth centuries AD (which involved emplacement of the Palizzi eruptive unit) was presented by Di Traglia et al. (2013). According to Di Traglia et al. (2013), the Palizzi Eruptive Unit was fed by summit vents and consisted of four explosive phases (PAL A to PAL D) and two effusive phases (that emplaced the Commenda rhyolitic lava and the Palizzi-Campo Sportivo-Punte Nere trachytic lavas). The entire cycle resulted in a significant growth in size and elevation of the cone itself (Di Traglia et al. 2013).

In the reconstructions of Keller (1980) and Di Traglia et al. (2013), the trachytic effusive phases of the Palizzi eruption consisted of the emission of the Punte Nere delta (east), the Campo Sportivo (north) and the Palizzi (south) lavas. On the other hand, De Astis et al. (2013) suggested based on previous datings that the Punte Nere lava were much older (4.6 ± 1.7 ka, Frazzetta et al. 1984; 5.3 ± 2.2/1.1 ka to 3.8 ± 0.9/0.8 ka, Soligo et al. 2000) than the Palizzi-Campo Sportivo trachytic lavas (1.6 ± 1.0 ka, Frazzetta et al. 1984; 1.5 ± 0.2 ka; Voltaggio et al. 1997). According to this scheme, the outpouring of the rhyolitic Commenda lava occurred between the Punte Nere and Palizzi events (2.2 ± 1.3 ka, Frazzetta et al. 1984; 2.1 ± 0.3 ka, Voltaggio et al. 1997; De Astis et al. 2013), whereas it postdates the Palizzi-Campo Sportivo-Punte Nere lavas according to Di Traglia et al. (2013). Its stratigraphic position still remains debatable, but all reconstructions agree that the Commenda lava is older than the BdC eruptive sequence.

The stratigraphic position of BdC deposits, in turn, is consistently on top of both the Palizzi and Campo Sportivo lavas (Supplementary Material). Although dating efforts are not in complete agreement (cf. Frazzetta et al. 1984; Soligo et al. 2000; Arrighi et al. 2006), the Punte Nere lava shares the same stratigraphic position (immediately below the BdC deposits) as, and have identical chemical compositions, the Palizzi and Campo Sportivo lavas, suggesting that it could have been emplaced in the same period (Supplementary Material). Whatever the case, at least two important lava effusions (Campo Sportivo and Palizzi) took place immediately before the BdC eruption, with the possible addition of the Punte Nere and Commenda lavas.

Methods

Stratigraphic logs and field observations were carried out at ~ 150 natural outcrops and at ~ 20 machine-excavated trenches at increasing distances from the La Fossa cone, where the current topography is flat enough to allow a good

Table 1 Main phases and stratigraphic features of the deposits related to the Breccia di Commenda eruption (the summary of Gurioli et al. 2012 is also reported for comparison)

Phases *Layers* (Gurioli et al. 2012)	**Phases** *(This work)*	**Layers** *(This work)*		***Description*** *(This work)*	
Phase 3 *Lithic ash fallout*	**Phase 3** *Final phase*	**Layer 3-rew** *Reworked deposit*	**Layer 3** *Lithic ash fallout*	**Layer 3-rew** **Lithofacies**: massive, chaotic deposits. Sandy matrix with pebble and boulder-size clasts. Locally massive, chaotic, hardened, mud deposits **Lithic clast type and shape**: Black-bluish, altered lavas, grey obsidian lavas; very altered, grey lavas; black, spherulitic obsidian lavas; very altered, black obsidian lavas, with grey flow-banding; black scoriae with red incrustation. The ash-matrix, if present, is red and constituted by altered clasts and crystals. Locally lithic mud **Thickness and dispersion**: 10–100 cm. Northern and north-eastern cone-base **Interpretation**: Reworked	**Layer 3** **Lithofacies**: parallel bedded, fine-ash layers. Each layer is massive. **Lithic clast type and shape**: Lithic ash **Thickness**: 20–30 cm **Other features**: Transition from accretionary lapilli-bearing to vesiculated tuffs layers **Interpretation**: Lithic ash-fallouts
Phase 2d *Lithic ash fallout*	**Phase 2d** *Lithic ash fallout*	**Phase 2d** *Lithic ash fallout*		**Lithofacies:** massive, fine-ash lenses **Lithic clast type and shape:** accretionary lapilli-bearing, brown-yellow, massive, well-sorted coarse ash **Thickness and dispersion:** 5–10 cm **Interpretation:** co-PDC deposits	
Phase 2c *Dense PDC*	**Phase 2** *Paroxysmal phase*	**Layer 2c** Dense PDC		**Lithofacies**: massive, chaotic, block-and-ash deposit (~ 5° slope angle). Fines-poor pipes (major valleys). Large boulder-size clasts (break in slope) **Lithic clast type and shape**: Black-bluish, altered lavas, grey obsidian lavas; very altered, grey lavas; black, spherulitic obsidian lavas; very altered, black obsidian lavas, with grey flow-banding; black scoriae with red incrustation. The ash-matrix, if present, is red and constituted by altered clasts and crystals **Thickness and dispersion**: up to 345 cm. Radial **Other features**: up to 1 m sub-rounded blocks with extensive external alteration. Absence of thermal contraction **Interpretation**: Dense PDC. Fluid escape dominated flow-boundary zone, turbulent shear induced tractional segregation. Major valleys: pipes due to vapour flashing in wet environment. Break in slope: localised current non-uniformity (depletive competence)	
Phase 2b *Dilute PDC*		**Layer 2b** Dilute PDC		**Lithofacies**: sequence of fines-poor and fines-rich cross-bedded, normal graded laminae **Lithic clast type and shape**: black-bluish, altered lavas, grey obsidian lavas; very altered, grey lavas; black, spherulitic obsidian lavas; very altered, black obsidian lavas, with grey flow-banding; black scoriae with red incrustation. The ash-matrix, if present, is red and constituted by altered clasts and crystals **Thickness and dispersion**: up to 50 cm. South-ward dispersion **Interpretation**: Dilute PDCs	
Phase 2a *Ballistics + dilute PDC*		**Layer 2a** Ballistics + diluted PDCs		**Lithofacies**: (*Basal lenses*) coarse-grained and fines-poor, discontinuous lenses or layers of coarse lapilli to boulder-size clasts; (*main deposit*) fines-poor, normal-to-reverse graded, clast-supported, continuous layer or discontinuous lenses. Diffuse-stratified, thin-bedded, not laterally persistent, low-angle truncations (small irregularities). Fines-poor, clast-supported, discontinuous lenses (large irregularities) **Lithic clast type and shape**: black-bluish, altered lavas, grey obsidian lavas; very altered, grey lavas; black, spherulitic obsidian lavas; very altered, black obsidian lavas, with grey flow-banding; black scoriae with red incrustation. The ash-matrix, if present, is red and constituted by altered clasts and crystals **Thickness and dispersion:** (*Basal lenses*) up to 30 cm diameter-clast. Radial, southeastern-ward dispersion; (*main deposit*) Up to 100 cm. Radial, south-ward and eastern-ward dispersion **Interpretation:** (*Basal lenses*) ballistics; (*main deposit*) Dilute PDC Main facies: high deposition rate Small-irregularities: subtle unsteadiness Large irregularities: reduction of flow competence due to 'blocking-effect'	

Table 1 (continued)

Phases *Layers* (Gurioli et al. 2012)	**Phases** *(This work)*	**Layers** *(This work)*	***Description*** *(This work)*
Phase 1 *Lithic ash fallout*	**Phase 1** *Opening phase*	**Layer 1b** *Lithic ash fallout*	**Lithofacies:** massive, fine-ash layer **Lithic clast type and shape:** Lithic ash **Thickness and dispersion:** 5 to 8 cm. South-ward dispersion **Other features:** S-bearing incrustations **Interpretation:** Lithic ash-fallout
		Layer 1a *Lithic ash fallout*	**Lithofacies:** massive, fine-ash layer **Lithic clast type and shape:** Lithic ash **Thickness and dispersion:** 1 to 10 cm. West-ward dispersion **Other features:** S-bearing incrustations **Interpretation:** Lithic ash-fallout

accumulation of both primary and secondary deposits. All the stratigraphic information is reported in a Google Earth© .kmz file where the sections with thickness of the various layers are detailed (see Online Supplement).

Bulk samples (of ~2 kg each) for layers 2b and 2c were first dried and then mechanically sieved from -4ϕ to 5ϕ at 0.5ϕ intervals (where $\phi = -\log_2 d/d_0$, d being the particle diameter and $d_0 = 1$ mm) for grain size analysis. To gain information on the source of the lithic material contained in the BdC deposit, we investigated the nature and the relative abundance of the different rock protoliths. At each locality, 100 clasts with diameters in the range 5–10 cm were randomly hand-picked. This clast size represents, on average, a small volumetric fraction of the bulk deposits (layers 2b and 2c) analysed for grain size. To classify rock fragments according to their lithology and composition, each fragment was broken in the field and observed with the aid of a hand lens. Plots of the data were expressed as percentage of different protoliths.

The volumes of the initial tephra fall deposits (layers 1a and 1b) were calculated following Pyle (1989) and Bonadonna and Costa (2012), and those of the PDC deposits were obtained by integrating the thickness variation of deposits. The PDC deposits derived from phase 2 (layers 2a and 2c) were sampled at 22 sites and processed for grain-size analysis. The new field and grain-size data were integrated with the dataset presented by Gurioli et al. (2012).

Both stratigraphic observations and field data were also used to infer the state of the summit area and shallow hydrothermal system before the eruption, its role in eruptive dynamics and as input parameters for physical modelling (see Appendix for model). The model applied in this paper aims at describing the paroxysmal stage of the eruption (phase 2). Our modelling, given in Appendix 1, considers the explosion dynamics and ballistic-block ejection, as well as the emplacement of layers 2a and 2b from turbulent, stratified PDCs.

The BdC deposits have inherent spatially non-uniform features and their structure (see 'Stratigraphy, sedimentology and analysis of the erupted products' section) suggests emplacement under strongly unsteady conditions, making simplified models difficult to apply. Moreover, the wide spectrum of grain sizes hinders the use of dusty-gas models, which cannot describe thermal and mechanical non-equilibrium processes. We therefore applied a transient, three-dimensional non-equilibrium Eulerian–Eulerian multiphase flow model (Neri et al. 2003; Esposti Ongaro et al. 2012) which as able to simulate the dynamics of the explosion, and a coupled Lagrangian model (de' Michieli Vitturi et al. 2010) to describe the trajectories of ballistic blocks. While the Eulerian formulation is more suited for a large number of particles, strongly coupled with the gas phase (i.e. for particles with diameters below about 1 mm), a Lagrangian approach is more appropriate for loosely coupled regimes (i.e. particles above a few centimetres; Cerminara et al. 2016). We have verified that the two formulations are equivalent (both physically and numerically) for particles in the lapilli range (2 to 64 mm). To solve the model equations numerically, we have developed a new solver with OpenFOAM, an open-source computational infrastructure for Computational Fluid Dynamics. The coupled model and the new numerical code are presented in detail in the Appendix.

The model assumes that the explosive phase 2 was triggered by the sudden exposure to atmospheric pressure of the shallow hydrothermal fluids, initially at high pressure and temperature. This is a 3D equivalent to the 'top-down' model for hydrothermal explosions by McKibbin et al. (2009), but the effect of the flashing of the superheated fluids and the subsequent downward migration of the boiling front are not taken into account here, as water is considered as already vaporised.

Stratigraphy, sedimentology and analysis of the erupted products

Our proposed stratigraphic reconstruction of the BdC event is similar to that proposed by Gurioli et al. (2012), from which

we take the distinction of the three main phases (phase 1, phase 2, phase 3) which can further subdivided into different layers (Fig. 2b). Based on stratigraphic correlations (Fig. 3) and considering the thickness variation shown by the lowermost unit (emplaced during phase 1, and hence representing the opening phase of the eruption), we define two distinct layers (1a and 1b) representing ash fallout deposits separated by the Rocche Rosse tephra and having different dispersal areas (Fig. 4a). The lowermost layer (layer 1a) has a westward dispersal, while layer 1b has a southward dispersal.

Deposits associated with phase 2 can be divided into four layers (2a through 2d). In agreement with the reconstruction of Gurioli et al. (2012), layers related to phase 2a are mostly dispersed in the south-eastern, eastern and north-western sectors. However, our reconstruction indicates an extension of the maximum distance attained by the ballistic blocks and the associated PDCs. Large ballistic blocks (up to 30 cm in diameter), accompanied by high concentrations of ballistic blocks per area (several blocks per square meter), were documented in the field up to about 2100 m from the crater (s151, Fig. 1c). The high concentration of impact craters produced by block fallout in the south-eastern sector of La Fossa cone resulted in a systematic disruption of the original ash fall succession at the base of the BdC sequence (Fig. 5a–c). Layer 2a consists of an ash-poor, topography-draping and filling, PDC deposit which was emplaced together with the ballistic block shower. This deposit covers more than 4.7 km^2 with a minimum volume of 2.8×10^6 m^3. In proximal to medial sites, PDCs and ballistic blocks are admixed together, suggesting that they were deposited almost simultaneously (Fig. 5c). It is worth noting that the blast-like nature of the layer 2a PDCs is confirmed by their capability to easily overpass a topographic barrier as high as 175 m at a distance from the source of about 2 km in the south-eastern direction. The thickness and coarse grain-size of layer 2a in the distal outcrop (s151, Fig. 1c) suggest that the dispersal of the PDC was greater than mapped here.

The layer 2a PDC was immediately followed by a PDC which emplaced an ash-rich, thinly stratified, dune-bedded deposit (layer 2b), with a thickness varying between 0.1 and 0.3 m but significantly less dispersed as compared to layer 2a (Figs. 4c and 5d). The different areal distribution of layer 2a (with a longer run out towards east and west) with respect to

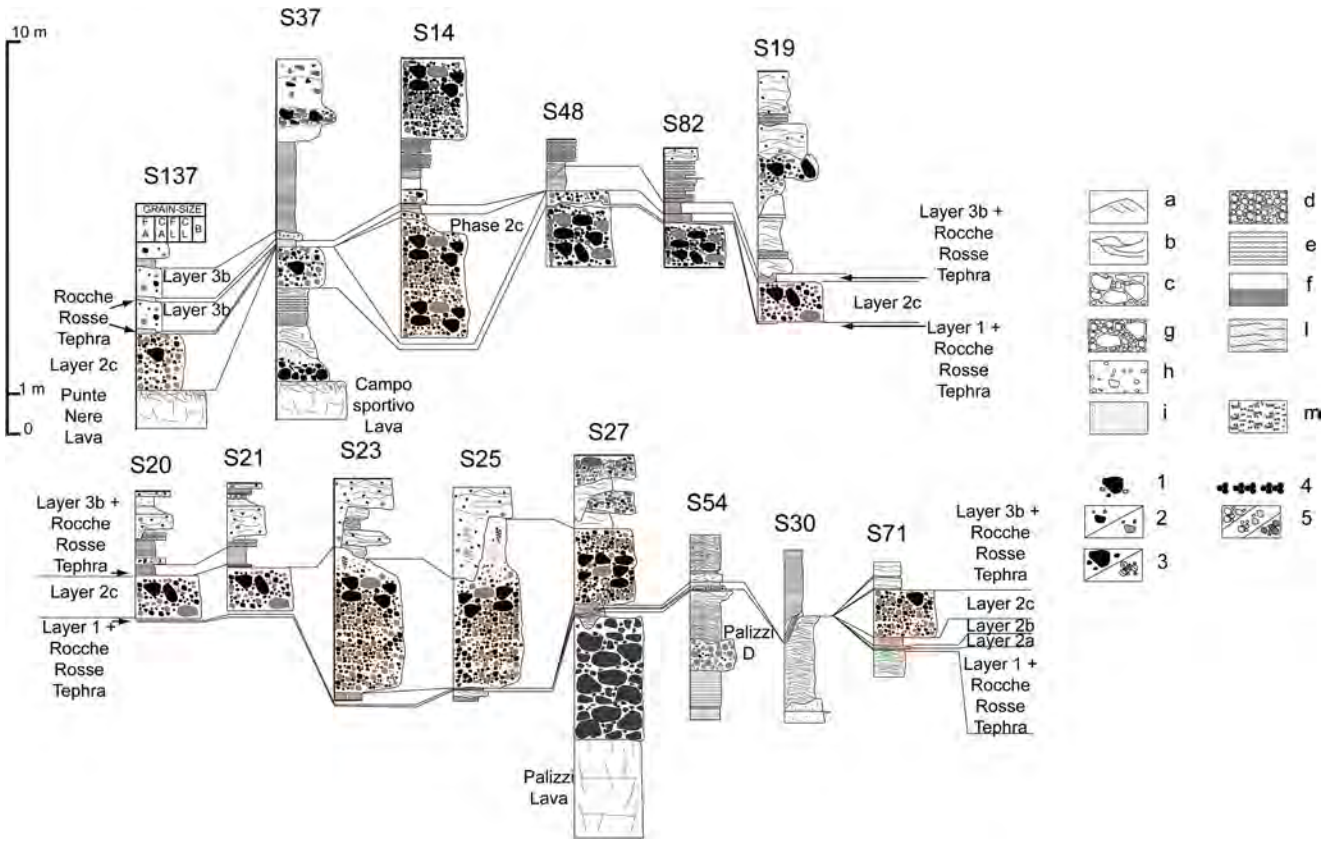

Fig. 3 Detailed stratigraphy and correlations among key stratigraphic sections: in the horizontal axes FA = fine ash; CA = coarse ash; FL = fine lapilli; CL = coarse lapilli; B = bombs and blocks. Lithofacies symbols: (a) cross-bedding; (b) irregular-bedding; (c) massive, unsorted; (d) massive, well sorted; (e) laminated; (f) thinly laminated; (g) massive, poorly sorted; (h) fine-grained, unsorted; (i) massive, fine-grained, well sorted; (l) wavy-bedded; (m) vesiculated; (1) mixed pumices-obsidian; (2) altered clasts; (3) banded clasts; (4) accretionary lapilli; (5) white/grey/golden pumices. Location of the sections is reported in Fig. 1

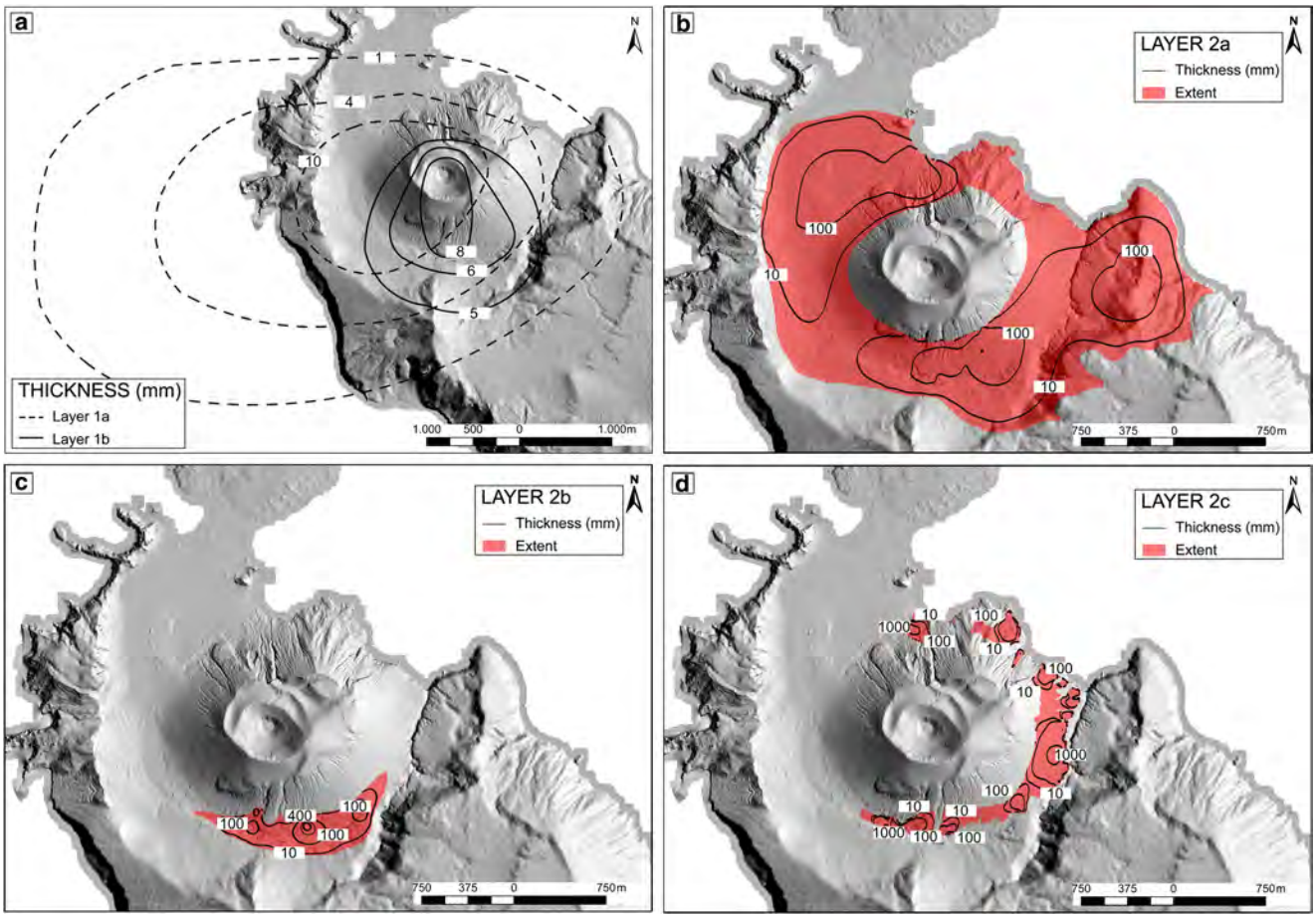

Fig. 4 Dispersal and thickness variations for **a** layers 1a and 1b, **b** layer 2a, **c** layer 2b and **d** layer 2c. Thicknesses are in millimetres

layer 2b (south-directed) suggests that the two layers might have originated from two different pulses in the eruption sequence that made up layer 2 (Fig. 4).

Phase 2c consisted of the emission of dense PDCs which led to the emplacement of massive deposits ranging from 0.8 to 3.5 m in thickness (layer 2c; Fig. 5d, e), mostly concentrated on the lowermost flanks and at the foot of La Fossa cone. They cover a total surface of 0.44 km^2 with a volume of 1.39×10^6 m^3. The distribution of layer 2c is neither regular nor ubiquitous around the cone (Fig. 4d), likely reflecting the vent location and the control played by the uneven height of the crater rim (i.e. the likely represent boiling-over activity, where directions of over-flowing PDCs are controlled by the geometry of the crater rim). The coarsest breccia deposit (with boulders up to 1.5 m in diameter) was observed along the shoreline between Punte Nere and Porto di Levante bay (Fig. 6a), suggesting that the BdC source vent was located close to the northernmost sector of the La Fossa crater area and that a part of the deposit likely entered the sea. In this area, and in the Palizzi valley, vertical, fines-poor pipe structures are abundant and well preserved in the deposit (s23 in Fig. 1c). Massive, boulder-rich (less than 1 m in diameter) breccia deposits are also present in the Palizzi valley at the break-in-slope at the foot of the La Fossa cone (Fig. 6b). On the south-eastern flank of La Fossa, layer 2c is overlain by an ash-rich, accretionary lapilli-bearing deposit (layer 2d) which possibly represents co-PDC deposits emplaced immediately after the breccia (Fig. 5f).

Phase 3 comprises grey to red ash fall deposits separated by at least three layers related to Rocche Rosse tephra. As described by Gurioli et al. (2012), these deposits have been observed dominantly in the southern and eastern sectors of La Fossa, suggesting dispersal towards the southeast. The lower part of phase 3 (layer 3a) is represented by a series of lithic-rich, 'wet' layers of vesicular tuff bearing non-structured accretionary pellets, which represent, waning, ash-emission, tail of the eruption (Gurioli et al. 2012). In the Palizzi valley and on the northern side of the La Fossa cone, the Rocche Rosse tephra layers are observed interbedded with a 1-m-thick, massive, matrix-supported ash and pebble deposits (lahar units; layer 3b). These stratigraphic features suggest that deposition and reworking of the primary ash fall occurred close in time.

Nature of lithic material in the BdC deposits

The deposits related to the BdC eruption are characterised by a large amount of lithic material, mostly consisting of angular

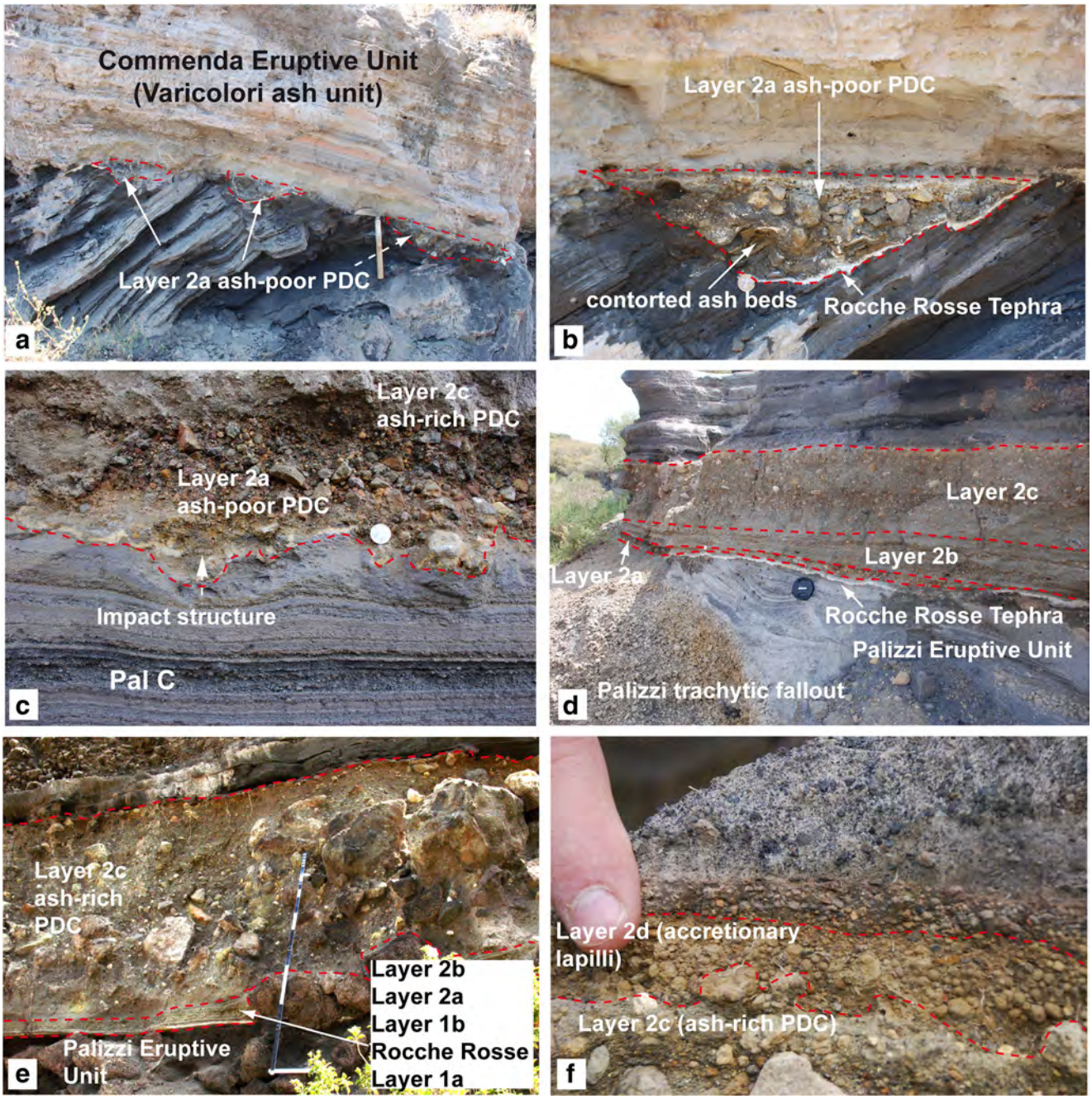

Fig. 5 Pictures of key outcrops for the BdC deposits. **a** The most distal outcrops of layer 2a (s153; refer to the Electronic Supplementary Material for location), **b** details of (**a**), highlighting the stratigraphic and geometric relationship between layer 2a and the Rocche Rosse tephra, as well as the coarse-grained and chaotic appearance of layer 2a. The presence of contorted ash beds, derived from the erosion of the underlying deposits (Palizzi Eruptive Unit), are also emphasised and are related to ballistic impacts. **c** Impact structures at the base of layer 2a in trenches in the south sector of the La Fossa cone (s148). **d** The occurrence of the layer 2b in the south-western part of the La Fossa cone (s71). **e** Massive lapilli tuff lithofacies in layer 2c (above the Palizzi lava flow; Frazzetta et al. 1983; s27); **f** accretionary lapilli rich lenses at the top of layer 2c (s71)

lava fragments (Fig. 6). Understanding the origin of this lithic material is thus crucial in understanding the structure of the summit area when the BdC vent opened, with a secondary aim being to locate the position of the vent during the eruption. To do this, we integrated the componentry analysis of the matrix (coarse ash) carried out by Gurioli et al. (2012) with a systematic observation of protoliths at key locations. The sampling sites, as well as the results of the classification and relative abundances of different rock types, are reported in Fig. 7. Results highlight that, at different sites, the relative abundances of different protoliths are comparable where the large majority of the examined rocks (56–70%) consists of lavas, ranging from fresh to poorly altered, and from dense to vesicular (Fig. 6e). All fresh and poorly altered lava clasts bear

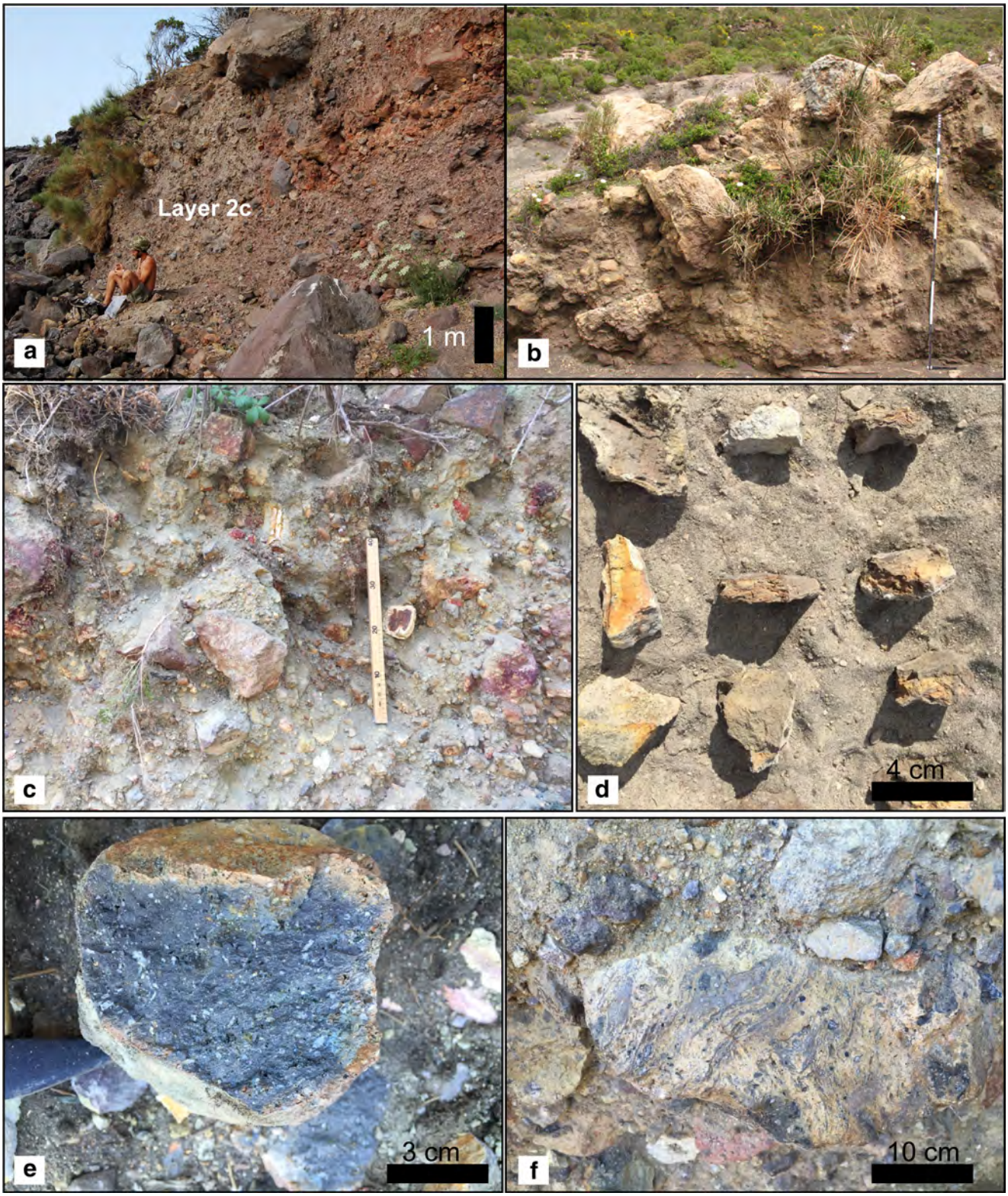

Fig. 6 **a** Outcrop showing the thickest and coarsest breccia deposit (boulders up to 1.5 m diameter) related to layer 2c, observed along the shoreline between Punte Nere and Porto di Levante bay (100 m south of section 5 in Fig. 7); **b** massive, boulder-rich (less than 1 m in diameter) layer 2c breccia deposits in the Palizzi valley (section 21 in Fig. 7), showing rock fragments in the topmost part of the deposits derived from incorporation in the flow by bulking processes of Commenda lava clasts; **c** degassing pipes structures in layer 2c (section 5 in Fig. 7). Tool for scale is 30 cm; **d** altered, oxidised, hard crust fragments within the most distal, southeast outcrop of layer 2a (section 153 in Fig. 7). **e** Dense to vesicular, fresh and poorly altered lava clasts, containing millimetre-sized crystals of feldspar and pyroxene in fine-grained groundmass (section 5 in Fig. 7); **f** welded scoria clasts within layer 2c close to the Porto di Levante area (section 5 in Fig. 7)

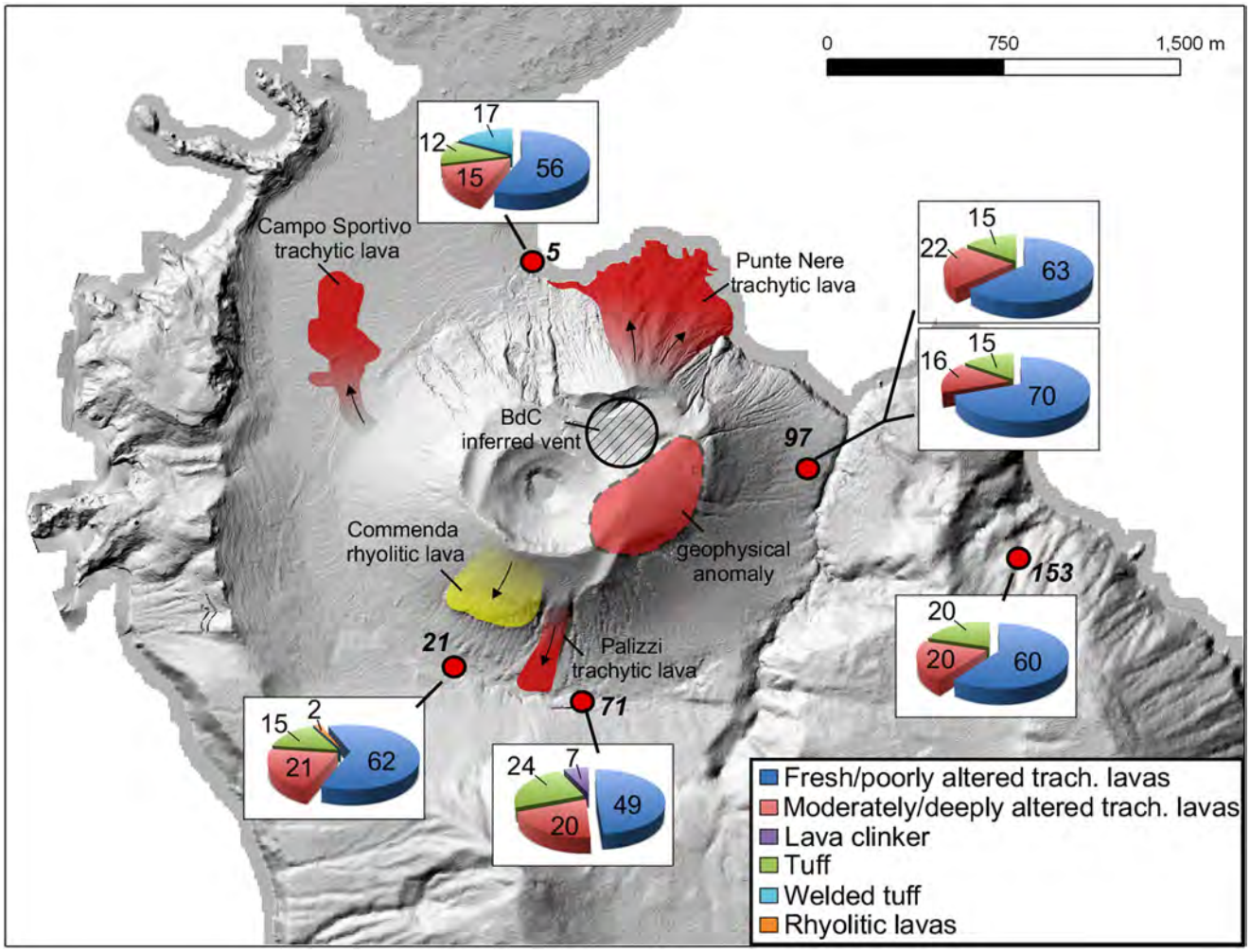

Fig. 7 Sampling site locations (in italics) and the results of the classification and relative abundances of different rock types, expressed as pie charts with percentage values. The dominant part of the material ejected during the BdC eruptive sequence consists of lava clasts with texture and composition similar to the trachytic lavas issued at the end of the Palizzi Eruptive Unit. Flow banded rhyolitic lavas (in orange) have been recognised only downslope of the rhyolitic Commenda lava

millimetre-sized crystals of feldspar and pyroxene set in a fine-grained groundmass consistent with an intermediate composition (trachyte). This category is followed in abundance (15–20%) by moderately to strongly altered lavas. The moderately altered lavas are also intermediate in composition (trachytic), the deeply altered lavas being difficult to classify. Hydrothermally altered tuffs were identified as the third most abundant category (15–24%).

Clasts of welded scoria were found only in the site north of La Fossa cone (15%), and flow banded rhyolitic lavas and fresh, trachytic lava clinkers were only sporadically present in the deposits located in the southern sites (Fig. 7). Because these less abundant rock types only occur at specific locations and each type is present only in outcrops located downslope of sites where the same rock crops out, we interpret their presence as due to incorporation of this material during flowage of the PDCs from the crater area towards the valleys (i.e. their presence results from a bulking processes). In support of this hypothesis, flow banded rhyolitic lavas are only present downslope of the rhyolitic Commenda lava, welded scoria downslope of the Punte Nere area and fresh trachytic lava clinkers downslope of the Palizzi lava flow.

Our analysis of the breccia protoliths, as well as that of Gurioli et al. (2012), suggest that (1) during the course of the BdC eruptive activity, a large volume of old material, especially lavas of shallow origin altered by fumarolic activity, was ejected; (2) the dominant part of these products consisted of lava clasts of trachytic composition, from fresh to moderately altered, with texture and composition similar to the trachytic lavas issued at the end of the Palizzi eruptive unit; (3) only a limited amount of the rock fragments in the breccia is constituted by clasts derived from material outcropping upstream of each sampling site; (4) the possible juvenile origin of a part of the fresh lava clasts seems unlikely as no evidence of rapid quenching (glass rinds or radial jointing) was detected in the analysed clasts. Moreover, no blocks or bombs show evidence of heating of the

surrounding finer matrix, as commonly seen in halos formed upon contacts of ash with bombs at nearly magmatic temperatures.

Grain-size analysis

In addition to the data derived from the 22 sites sampled in this work (Fig. S6 in the Supplementary Material), data from Gurioli et al. (2012) were used to depict the overall grain-size characteristics of PDC deposits related to phases 2a and 2c (Figs. 8 and 9). Grain-size data of layers 2a and 2c form two discrete groups on both the Mdϕ (median)–$\sigma\phi$ (sorting) and F1 (% fraction ≤ 1 mm)–F2 (% fraction ≤ 1/16 mm) diagrams (Fig. 8). Mdϕ of layer 2a varies from − 5.1 to 2.1ϕ, whereas $\sigma\phi$ varies from 1.2 to 3.4. F1 accounts between 90.9 and 5.5% and F2 represents from 0 to 9.8% of the total. In contrast, layer 2c is distinctive because of its lower sorting, irrespective of absolute grain size. The deposit also shows the largest range in Mdϕ (from − 5.8 to 3.2ϕ), $\sigma\phi$ (1.4 to 3.7), F1 (17.0 to 95.6%) and F2 (0.2 to 33.0%). Layer 2a is thus generally better-sorted with respect to layer 2c, with an evident lack in fine (< 0.063 mm) material, and having a unimodal distribution (Fig. 8). On a plot of F1 versus F2, samples of layer 2a occupy the area below the field of PDCs (Fig. 8b), indicating either a reduced fragmentation at the source vent or a significant depletion of fines during transport, or both. The grain-size distribution of layer 2a is similar to that of high-energy blasts deposits (i.e. layer B, defined as 'strongly depleted by fines and thus has a clast-supported fabric with open voids between clasts' in Belousov et al. 2007), such as the 1902 Mt. Pelee (Martinique; Lajoie et al. 1989), 1957 Benzymianny blast (Russia; Belousov 1996), the 1980 Mount St. Helens blast (USA; Hoblitt 2000) and the Boxing Day, 1997 Soufriere Hills blast (Montserrat; Ritchie et al. 2002). In particular, it shows close similarities with the hydrothermal blast deposit produced during the 2012 Te Maari eruption at Mt. Tongariro (New Zealand; Lube et al. 2014).

Compared with typical pumice-rich, high-concentration PDC deposits (Fig. 8a), layer 2c is relatively ash-poor and relatively well sorted, likely reflecting the weaker fragmentation of lithic material compared to fragile highly vesicular pumice both at the source vent and during transport. Fragmentation during transport of PDC 2c had a limited role as all PDCs travelled less than 1300 m from the summit of the La Fossa cone.

Modelling the explosion dynamics of the *BdC* eruption

Based on the observation that a phase of effusive activity shortly preceded the BdC eruption, and on the character of the lithic material which largely comprises the breccia deposit, we assumed that the exploding volume was initially confined within the La Fossa cone crater area, which was possibly filled by lava from the previous effusive eruptions. Magma degassing through the volcaniclastic material from previous eruptions and the overburden of the crater-filling lavas provided the necessary conditions for the build-up of the interstitial gas overpressure. This scenario is compatible with continuous degassing, including fumarolic. When this fluid overpressure exceeded the tensile strength of the overlying lava cap, a breakdown occurred (not modelled here), exposing the porous material and hydrothermal system fluids to atmospheric pressure. The explosion was then driven by the rapid decompression of the fluids and the fragmentation of the porous material into a gas–particle mixture, made up of water vapour, ash and lithic blocks. This was subsequently accelerated during expansion in the atmosphere. In this stage, the blocks were ejected ballistically from the vent, while the ash fraction was mechanically coupled with the eruptive plume. Lateral expansion and the rapid collapse of the gas–particle jet generated turbulent PDCs. The numerical model used in this work aims at simulating the event starting from the decompression and acceleration

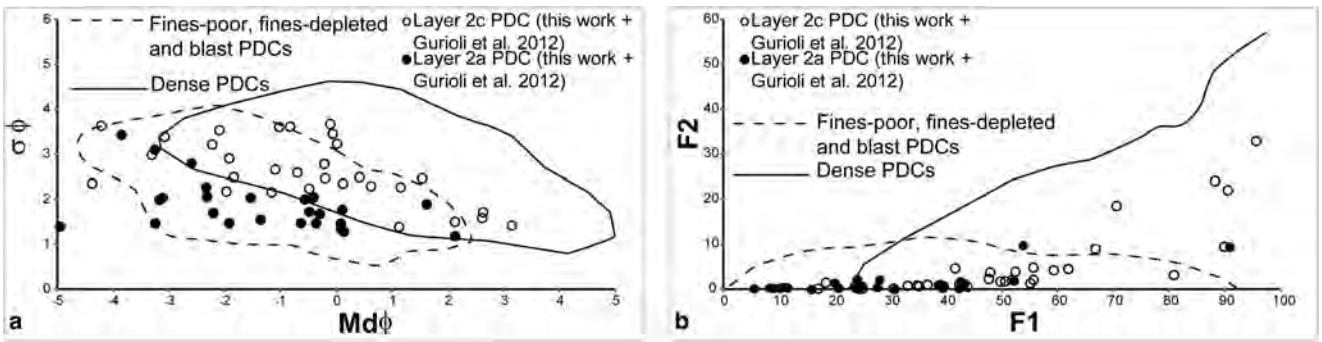

Fig. 8 Grain-size features of BdC deposits, using both data from this work and from Gurioli et al. (2012). **a** Mdφ vs. $\sigma\varphi$ diagram (Walker 1971) and **b** F1 vs. F2 diagram (Walker 1971) of layer 2a and layer 2c, showing the lack of fines, as also observed in other fines-depleted, fines-poor and blast deposits (data from Boudon and Lajoie 1989; Brissette and Lajoie 1990; Yamamoto et al. 1999; Ritchie et al. 2002; Belousov et al. 2007; Lube et al. 2014; curves from Ritchie et al. 2002)

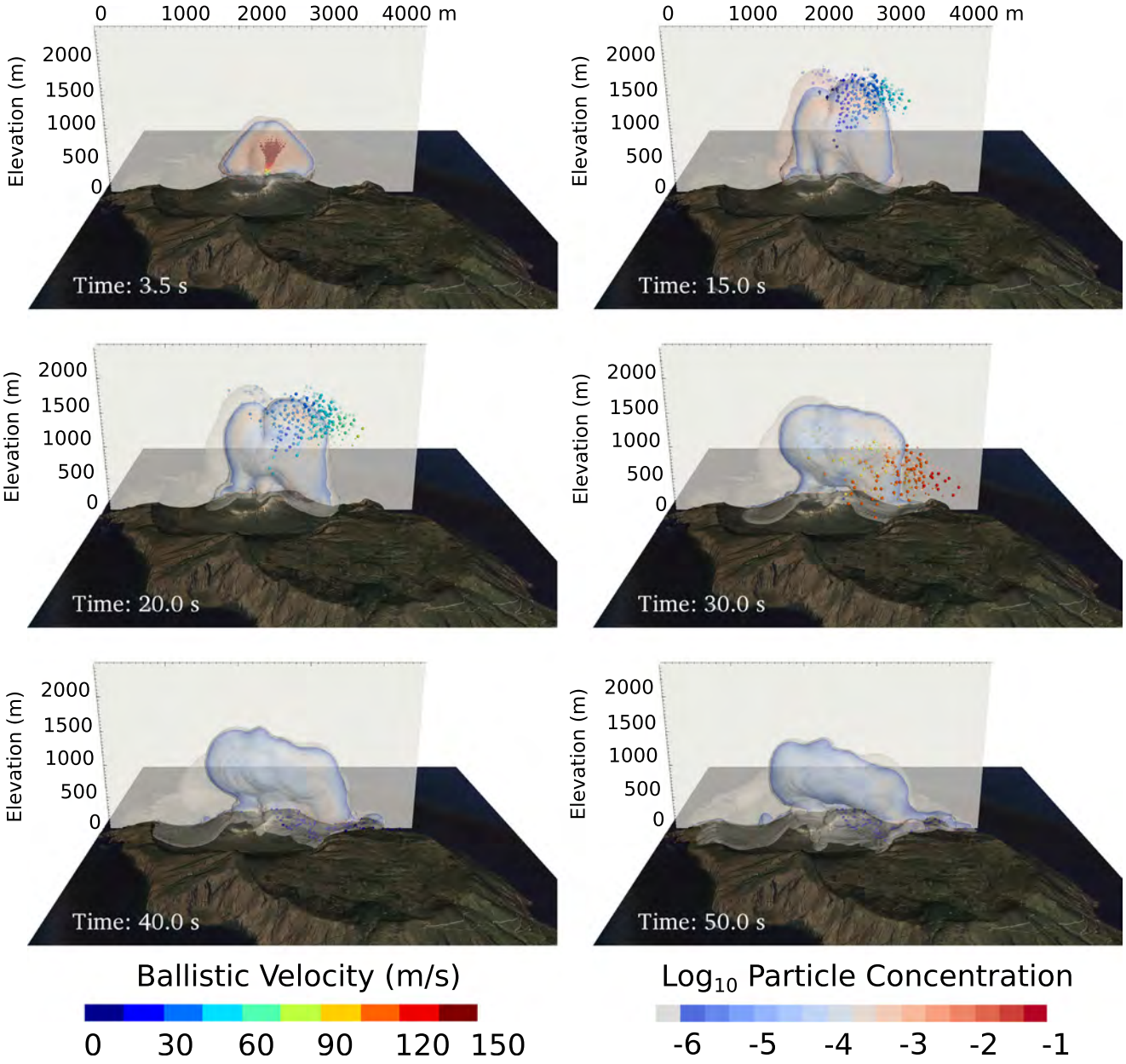

Fig. 9 Three-dimensional view of the eruption sequence after 3.5, 15, 20, 30, 40 and 50 s. Colour scale represents the logarithm in base 10 of the pyroclasts concentration (alpha), along a W–E section and at ground level. Ballistic particles of 8, 16 and 30 cm are drawn with different diameters and coloured depending on their velocity

of the mixture of overpressurized fluids and the already fragmented material, described by a Eulerian ash + lapilli fraction and a Lagrangian block-particle fraction (Neri et al. 2003, Esposti Ongaro et al. 2012; de' Michieli Vitturi et al. 2010).

Recent field/experimental studies have addressed some of the parameters controlling the dynamics and energetics of explosions due to decompression of a hydrothermal system, including the type of rock involved in the eruptive event and its porosity, permeability and strength, as well as the type and amount of fluid involved in the explosion and initial pressure-temperature (*P*–*T*) conditions. For the Te Maari case, experimental works have thus been conducted in a range of temperatures (200–350 °C), pressures (4–6.5 MPa) and lithology (Montanaro et al. 2016c).

We apply a parametric approach, focusing on the three parameters that mostly control the dynamics of the explosion of a pressurised shallow body of mass (*M*): the initial pressure (P_0), gas content (*n*) and temperature (*T*). The total erupted mass in phases 2a + 2b ranges (Table 2) from 7.5×10^8 kg (3×10^5 m^3 Dense Rock Equivalent, DRE) to 2.5×10^9 kg (10^6 m^3 DRE), with the lower bound being constrained by the measured volume of the pyroclastic deposit, and the maximum value estimated by considering mass not deposited or eroded.

Table 2 Physical parameters of layers 2a and 2c PDC deposits

Parameters	Layer 2a	Layer 2c
A (km^2)	4.68	0.44
V ($\times 10^6$ m^3)	2.71	1.39
L (km)	1.7	1.28
H (km)	0.38	0.38
H/L	0.224	2.97
λ	1.62	0.271
$A/V^{2/3}$	668	216
N_f	2.93×10^4	4.08×10^3

A area, V volume, L length (measured following Hayashi and Self 1992), H height (measured following Hayashi and Self 1992), λ ratio of the average width to the length of an avalanche deposit (Dade and Huppert 1998), N_f friction number ($A^{3/2}/\lambda^{3/2}\,V$; Dade and Huppert 1998)

The initial gas mass fraction (n) is related to the porosity of the exploding material (ϕ) by:

$$n = \frac{\phi\rho_g}{(1-\phi)\rho_s + \phi\rho_g}$$

where ρ_g is the density of the gas phase and ρ_s is the density of the solid phase, with $\rho_g = \frac{P}{RT}$, with P, R and T being pressure, the specific gas constant and temperature, respectively. We vary the porosity of the exploding body in a realistic range, from 0.3 to 0.7 (this is intended as a cell-averaged value for the hosting system, not the porosity of individual clasts). Based on experimental works by Montanaro et al. (2016c), overpressure is varied from 6.0 to 20.0 MPa. Mixture temperatures of either 523 or 623 K have been considered (250–350 °C).

The available specific energy (per unit of mass) for an adiabatic (but almost isothermal) explosion depends on the amount of compressed interstitial gas and can be estimated as (Wilson 1980):

$$E_{iso} = nRTln\left(\frac{P_0}{P_{atm}}\right) \cong \frac{1}{2}U^2$$

where R is the gas constant, n is the mass fraction of gas, P_0 is the pressure at the vent, P_{atm} is the atmospheric pressure and U is an estimate of the ejection velocity. For the reference case (Run F-N35E in Table 3), $E_{iso} \cong 54 \times 10^3$ J/kg, corresponding to an (over)estimated ejection velocity of about 320 m/s. In fact, in our simulations, ballistic blocks never reach such a velocity, due to the rapidity of the gas decompression and the delay in particle coupling.

The Digital Elevation Model with a spatial resolution of 1 m of the present island of Vulcano is used, but with the crater filled to the rim by pre-BdC lavas and a shallow, elongated fissure excavated within it. Such a geometry was chosen because we observed that it favours the generation of asymmetric PDCs and ejection of ballistic blocks in the direction orthogonal to the fissure main axis, as observed in the field. The width and depth of the fissure is set to fit the measured total mass (or DRE volume) of the eruptive products. The fissure is filled with a compressed gas–particle mixture, thus assuming that the eruptive mixture immediately fragmented during decompression (as in Clarke et al. 2002). Because the energy of fragmentation (1.8–4.8 MPa; Spieler et al. 2004; Mayer et al. 2016; Montanaro et al. 2016c) in the envisaged porosity range is lower than the assumed overpressure (12 MPa), this is equivalent to a maximum underestimation of 40% of the initial pressure needed to trigger the explosion (see also Esposti Ongaro et al. 2012). In addition, altered rocks can have lower fragmentation thresholds (up to 50% lower; Mayer et al. 2016; Montanaro et al. 2016c).

Finally, the Eulerian–Eulerian eruptive mixture in our model is represented by one gas phase and one particle phase of 2 mm diameter. The Eulerian particle phase should be considered as a hydraulically equivalent particle class representing pyroclasts in the ash–lapilli range (simulations with particles of 1 or 4 mm do not show significantly different explosion dynamics; Esposti Ongaro et al. 2012). Three ballistic-block classes of 8, 16 and 30 cm diameter (based on our field measurements) were used as Lagrangian phases.

Numerical simulation results

Figure 9 and Supplementary movie 1 depict the temporal and spatial evolution of the eruptive mixture made of gas, ash particles (2 mm) and blocks (8–30 cm) obtained from the numerical model. During the first 3–4 s (Fig. 9), the mixture expands almost isotropically, due to the dominant effect of the high-pressure gradient. This is the stage of rapid decompression (the *burst* phase of Esposti Ongaro et al. 2012) which is able to accelerate the mixture up to vertical velocities slightly exceeding 200 m/s. These are higher than those measured in analogous laboratory experiments (around 160 m/s; Montanaro et al., 2016c) probably due to the lack of the material yield strength and higher initial pressure. Blocks accelerate to comparable velocities of gas and lapilli due to drag forces and pressure gradient. Lateral surge velocity is, during this stage, of the same order of magnitude, and asymmetry/anisotropy of the fissure can direct ballistic blocks in preferential directions. In this case, ballistic blocks located initially in the centre and along the eastern margin of the fissure are preferentially driven towards the ESE.

After the burst stage (from 5 s to about 15 s, Fig. 9), compressibility effects (shock waves) create a vent-ward atmospheric motion that arrests the lateral surge motion and pulls the plume upward. In this stage, the fissure shape plays an essential role, as the 'suction' effect occurs only along the

Table 3 Geometric parameters and initial conditions of numerical simulations

Run	Geometry					Mixture properties					Collapse	Ballistic range
	R (m)	L (m)	B (m)	sh	V (m^3)	ϕ_s	n %	T (K)	P (MPa)	M_s (kg)		D (km)
C1*	100		200	1	2.0e06	0.3	7.5	523	12.0	1.5e09	Full	[1.15; 1.40; 1.65]
C2*	100		200	1	2.0e06	0.3	5.8	673	12.0	1.5e09	Full	[1.25; 1.45; 1.65]
C3*	67		268	2	1.6e06	0.3	7.5	523	12.0	1.0e09	Minor	Exit top boundary
C4	67		268	2	1.6e06	0.6	1.8	523	12.0	1.9e09	Partial	Exit top boundary
F-N45E*	40	200	160	1–10	2.1e06	0.3	7.5	523	12.0	1.6e09	Full (asymmetric)	[1.45; 1.70; 1.95]
F-N35E**	40	200	160	1–10	1.9e06	0.3	7.5	523	12.0	1.4e09	Full (asymmetric)	[1.25; 1.70; 2.00]
W1*	40	200	160	2	2.4e06	0.3	7.5	523	12.0	1.8e09	Partial (E–W)	[1.40; 1.70; 1.90]
W2	40	200	160	2	1.6e06	0.3	6.3	623	12.0	1.2e09	Partial (E–W)	[1.45; 1.70; 1.90]
W3	40	200	160	2	2.5e06	0.5	3.2	523	12.0	3.1e09	Full	[1.40; 1.10; 1.20]

Run names indicate circular vents (C), fissure (F) or wedges (W). (*) indicates runs carried out with and without the added pressure gradient term in the Lagrangian equations. (**) indicates simulations with vent located NE of the present crater (as in Fig. 7). R is the fissure radius or half-width; L and B are the fissure length and depth, respectively; sh is the shape of the fissure (1 = cone; 2 = paraboloid; 1–10 indicates an asymmetric fissure); V is the fissure volume. Symbol ϕ_s denotes the solid particle fraction (i.e. 1 minus the porosity of the exploding mass), n is the gas mass fraction, T the mixture temperature, P the initial pressure, M_s the total solid mass involved in the explosion, D indicates the distance reached by ballistic particles towards the East

direction of the fissure. Orthogonal to the fissure, the mixture collapses under the effect of gravity, forming PDCs. At the same time, ballistic blocks have reached their maximum altitude and decouple from the gas–particle mixture (typically particles > 8 cm in our simulations), spreading radially under the dominant effects of inertia and atmospheric drag forces. After reaching a maximum height of about 1500 m above sea level, the whole eruptive plume collapses, generating a second, major PDC, preferentially directed orthogonal to the fissure direction. At 40 s after the beginning of the event (Fig. 9), almost all ballistic blocks have landed, while PDCs are still propagating. The maximum distance reached by ballistic blocks of up to 30 cm diameter, ejected towards the East, is comparable with that observed in the field (2 km). The maximum flow run-out (> 3 km orthogonal to the eruptive fissure and 1.5 km along the fissure direction) is then reached after about 60 s.

Numerical simulations demonstrate that the observed PDC deposits and ballistic-block ranges are consistent with an erupting mechanism driven by the explosion of a shallow (non-magmatic) pressurised body. Different initial fissure geometries were tested in this work, both circular and elongated, and with different aspect ratios. Circular vents produce axisymmetric ejection, while explosions that were too shallow (less than 100 m) were too short-lived to accelerate ballistic fragments sufficiently to fit the observed ranges. Our best match is thus obtained with explosions from an elongated, asymmetric body measuring about 200 m in length and 80–100 m in width, located northeast of the present crater. With the imposed volumetric constraint, this results in a 150–180 m fissure depth. Although errors are very difficult to estimate systematically, the parametric study suggests a mass of $1.5 \pm 0.5 \times 10^9$ kg, an initial overpressure of 12 ± 3 MPa, a maximum temperature of 250 ± 50 °C and an initial porosity between 0.3 and 0.6. It is worth remarking that simulations with higher temperature of the exploding mixture tend to be more convective, hindering the formation of intense PDCs. This observation supports the idea that the involvement of significant amount of fresh magma is unlikely in this stage since it would have significantly raised the initial temperature of the system.

Discussion

Dynamics of the BdC eruption

The BdC eruption started with two distinct lithic-rich ash emissions (phases 1a and 1b). The onset of the eruption at La Fossa was pene-contemporaneous with explosive activity at the Rocche Rosse vent on Lipari Island (Fig. 10). The eruption suddenly escalated to its paroxysmal stage (phases 2a and 2b) consisting of the ejection of ballistic blocks mainly directed SE and in the flow of unsteady, stratified PDCs across the entire central sector of the La Fossa caldera. Layer 2a consists of an ash-poor, topography-draping, blast-like deposit which was emplaced together with the ballistic block shower. The blast was immediately followed by surge-like PDCs which emplaced ash-rich, thinly stratified, dune-bedded deposits (layer 2b). Gurioli et al. (2012) reported PDC deposits of layer 2a only confined to the southern and eastern sectors. The 17 new stratigraphic trenches that we dug around La Fossa cone

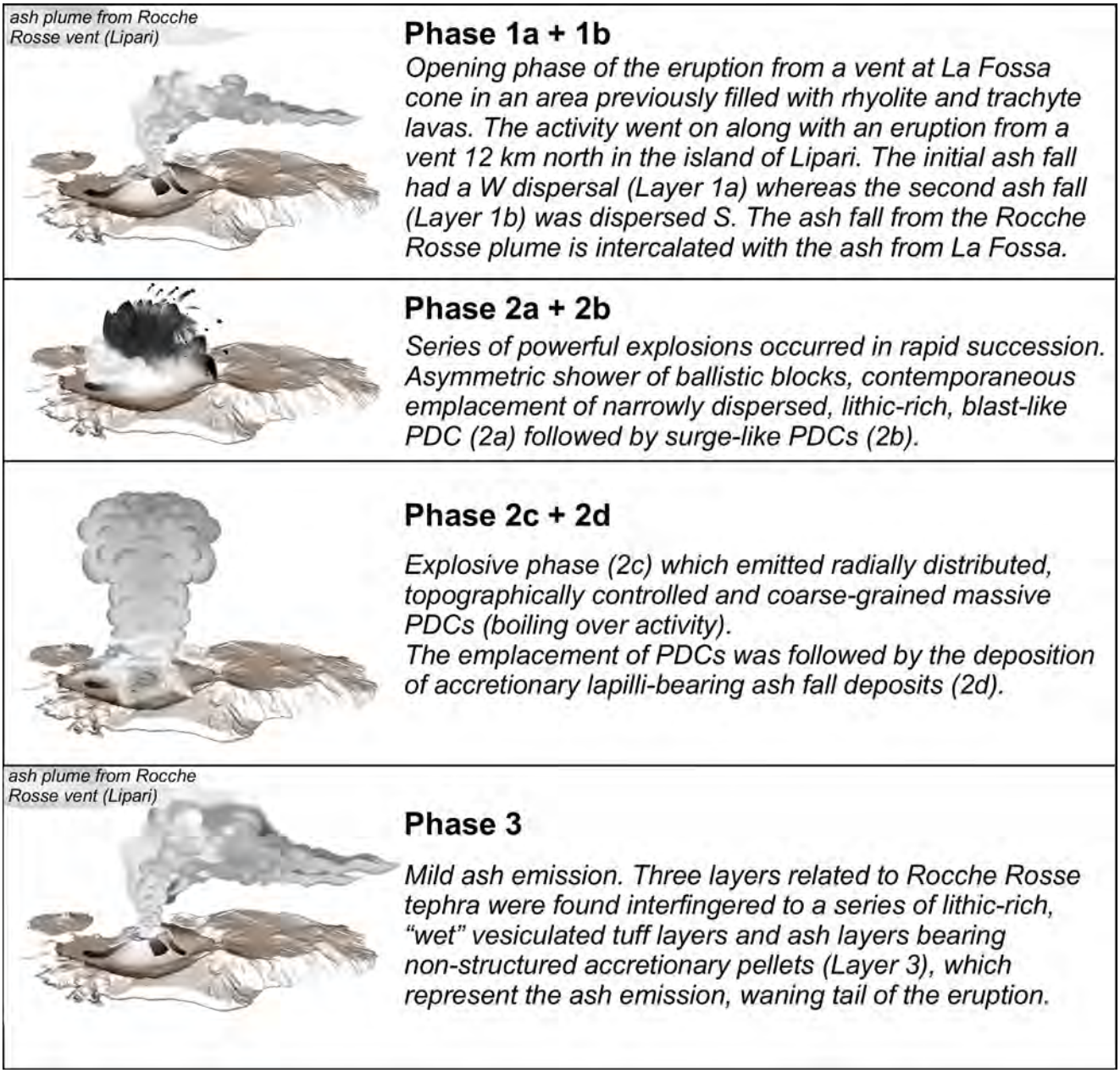

Fig. 10 Schematic reconstruction of the BdC eruption

allow us to extend this limit beyond the La Fossa caldera walls, highlighting also a north-western and south-eastern dispersal. Dense, gravity-controlled PDCs (layer 2c) were next generated. These were immediately followed by the accumulation of co-PDC, accretionary lapilli-bearing, ash deposits (layer 2d). The descent of the dense PDCs of layer 2c occurred only through the lower parts of the crater rim, suggesting that the PDC generation mechanism was by boiling-over activity. Regularly spaced, vertical, fines-poor pipe structures are abundant in the Palizzi valley and in the outcrops of layer 2c situated in the easternmost part of the Porto di Levante bay (Fig. 6c). Degassing structures are suggestive of a sudden deflation of fluidized PDC masses as they came to rest at the foot of the cone, possibly combined with a phenomenon of gas release from porous lithic clasts following the sharp decompression due to explosion. The observation reported by Gurioli et al. (2012), of vertical pipe-like structures originating from large, lithic, hydrothermally altered blocks of layer 2a, and crossing the deposit of layer 2b, suggests that the emplacement of layers 2a and 2b occurred close in time, as fluids were still being vigorously released from porous lithic clasts of layer 2a by the time the ash-rich layer 2b was deposited. On the other hand, the burial of the same degassing structures by layer 2c is indicative of a longer time interval between the emplacement of layers 2b and 2c. We hypothesise that the increase amount of fine (< 0.063 mm) material, from layers

2a to 2c, is related to the different rock lithologies within the crater. Initially, the ejection of the lavas topping the source area produced coarse-grained, fines-poor deposits (layer 2a), later the eruption disrupted the underlying poorly consolidated and altered tuff deposits, generating a higher amount of fine material (layers 2b and 2c).

In the final phase, BdC fallout deposits are interfingered with at least three Rocche Rosse tephra beds from Lipari. This clearly testifies that explosive activity in Lipari and Vulcano went on for some time contemporaneously. The ash deposit rich in accretionary lapilli (layer 2d) was likely due to secondary explosions produced by the vapour generated by the entrance of PDCs into the sea, as already observed at Soufriere Hills volcano, Montserrat (e.g. Mayberry et al. 2002; Carn et al. 2004; Burns et al. 2017). In contrast, the presence of non-structured ash pellets within the vesiculated tuffs of phase 3, coeval with reworking processes, suggests that wet environmental conditions affected both the eruptive plume and the emplaced ash deposits, eventually triggering lahars in the north-eastern sector and creating small mud ponds in the Palizzi valley.

Some controversial hypotheses exist in the literature regarding the presence of juvenile material in the BdC deposits. In fact, while Frazzetta et al. (1983), De Astis et al. (2006, 2013) and Dellino et al. (2011) propose that no juvenile fraction can be clearly identified, Gurioli et al. (2012) suggest that fresh glass material showing a large chemical variability from rhyolitic to trachyandesite does occur mostly in the finer fraction of the deposits (ash and lapilli) as well as in some bombs. This material, which is commonly below 40 vol.% of the deposits, frequently has fine ash adhering to grain surfaces and filling vesicles, with glass shards characterised by altered patinae. We did not identify a clear juvenile fraction in the coarsest clasts of the deposit, which also show no evidence of rapid quenching or interactions at high temperatures with the embedding, cooler finer matrix. Although definitive proof for either demonstrating or excluding the involvement of fresh magma in an eruption is not always straightforward, it has been recently pointed out that the presence of wide ranges of glass compositions (partially overlapping those of vent-area country rock), microlite textures and mineral content variability in glassy particles of deposits related to events with a strong hydrothermal signature is difficult to reconcile with involvement of fresh magma (Pardo et al. 2014). In fact, while several eruptions at La Fossa are heterogeneous because of mingling and mixing processes of small magma batches (Gioncada et al. 2003), these commonly show a predominant composition with minor contributions recorded as enclaves, while in the BdC event the chemical variability appears to be equal in volume, at least for the trachytic to rhyolitic end-members (Gurioli et al. 2012). If the eruptive mixture included a minor juvenile fraction of variable composition of sufficient volume to flash the hydrothermal system, this was small and cannot be unequivocally identified in the emplaced deposits.

Pre-eruptive state of the crater area and location of the BdC vent

Stratigraphic observations coupled with the recent reconstructions of the Palizzi eruptive period (Di Traglia 2013; De Astis et al. 2013) clearly show that the final eruptive period immediately before the BdC eruption consisted in a phase of effusive activity. The tight time relationship among the lava effusions and the BdC event is further constrained by the absence of lithic lava clasts in the previous PAL D fallout deposit, and by the lack of significant primary deposits between the lavas and the BdC tephra sequence (Supplementary Material). The state of moderate alteration of the lava fragments in the BdC deposits (fresh and moderately altered fragments account for more than 60% of the studied blocks) is also in agreement with a short time lapse of exposure to fumarolic action (about a century and a half) between the emplacement of lavas and their ejection as lithic material within the BdC deposits. The roots of the Palizzi and Commenda lavas can be nowadays clearly seen in the inner part of the present crater rim to be immediately below the BdC sequence. Moreover, geophysical surveys also revealed the presence of a buried lava body in the south-eastern part of the La Fossa cone (Fig. 7; Blanco-Montenegro et al. 2007; Barde-Cabusson et al. 2009; Napoli and Currenti 2016). In particular, Barde-Cabusson et al. (2009) suggested that the minimum depth of the geophysical anomaly can be estimated to ~ 50 m, in the range of the tephra pile emplaced after the Palizzi eruptive Unit (Commenda Eruptive Unit and Gran Cratere Eruptive Cluster; Di Traglia et al. 2013). All this evidence supports the idea that the final effusive activity immediately before the BdC event clogged the crater area with lava. This hypothesis is also supported by comparison of the volume of the lava material forming layer 2a (2.8×10^6 m^3 by considering the whole deposit as entirely made by lava lithics) with that of a hypothetical lava cap having a diameter comparable with the present crater geometry (600 m) and an average thickness of 10 m.

The presence at the end of the Palizzi eruption of lava in the summit part of the cone, which eventually flattened the summit area, can also explain the decrease of gas permeability and build-up of the overpressure necessary to overcome the tensile strength of rocks in the initial part of the explosion. The estimated overpressure from numerical modelling (12 ± 3 MPa) is consistent with values associated with the combined effects of the increased lithostatic load due to the lavas filling the crater ($P_L \sim 3.5$ MPa assuming a depth of the lava filling the crater $H = 200$ m and a density of 1750 kg/m^3) plus the pressure associated with magmatic gas flux through the porous matrix ($P_G \sim 10$ Mpa for a permeability of degassed lavas of 10^{-12}, according to Woods et al. 2002).

Regarding the location of the BdC vent, we suggest a possible location in the north-eastern sector of the La Fossa cone. This hypothesis is supported by the presence of the largest boulders (more than 1 m in diameter) observed in the northern

outcrop near the coast (Fig. 6a). Moreover, the agreement between field data and numerical simulations of phase 2a is more consistent with this location of the fissure vent.

Limitations and constraints of current modelling approach

Concerning the above model-derived pressure estimates, two additional factors should be considered. On one hand, depending on the amount and temperature of the available liquid water, the energy for fragmenting and sustaining the explosive phase might be much higher if steam-flashing was considered. This in turn would affect the efficiency in producing fine material which could feed both PDCs and ash plumes (Mayer et al. 2016; Montanaro et al. 2016a,c). In such a case, it is likely that the overpressure required to produce the observed phenomenology would be significantly lower. On the other hand, if the effect of the cohesive stress was taken into account (McKibbin et al. 2009), the required initial overpressure would increase. The balance between these two factors is difficult to estimate. However, accurate measurements of rock porosity/permeability together with constraint of rheological properties will likely help to add further constraints to the estimated initial pressure.

Comparison with other phreatic/hydrothermal eruptions

The blast phase of the BdC eruption (phase 2a) shows strong similarities with recent events directly observed at Soufrière-Guadeloupe (14 September 1976 blast; Sheridan 1980; Hincks et al. 2014), Te Maari-Tongariro (6 August 2012; Lube et al. 2014) and Ontake (27 September 2014; Maeno et al. 2016). Deposit characteristics of the BdC blast also resemble that of other historic events such as Zao 1895 (Fujinawa et al. 2008; Miura et al. 2012), Bandai 1888 (Yamamoto et al. 1999; Fujinawa et al. 2008) and Adatara 1900 (Fujinawa et al. 2008). Hydrothermal/phreatic blasts can occur as isolated events with little or no precursors (as at Bandai, Te Maari-Tongariro, Ontake) or within a phase of volcanic unrest (as at Zao, Adatara and Soufrière-Guadeloupe). The BdC eruption apparently belongs to the second category, showing an initial weak ash emission (phases 1a and 1b) preceding phase 2a (the blast phase).

The features of the blast phase are also similar to those described for other hydrothermal eruptions, in terms of the lithic-rich nature of the components, volume of the products (between 10^{-6} and 10^{-3} km^3), short duration of the events and strong directionality of the explosions, especially for the ballistic blocks and dilute PDCs (Table 4). Simulated PDCs propagate as turbulent, stratified currents, with maximum ash volume concentration of about 0.005. Their maximum temperature is higher (exceeding 200 °C) than that observed at Ontake (where temperatures within the PDCs were mostly below 100 °C), probably due to the more dilute conditions (Maeno et al. 2016), but they are consistent with those measured at Te Maari (about 280 °C; Lube et al. 2014), indicating that the initial temperature of the hydrothermal body is conserved during the blast phase (Esposti Ongaro et al. 2012). This is also similar to the average fumarole temperature currently measured at La Fossa, which is further support for our hypothesis. While there is little sedimentological evidence of PDCs associated to phreatic and hydrothermal events (because their small volume and thickness hinder their preservation), high-energy, dilute and low-temperature PDCs associated with explosion of a hydrothermal system should be more common than previously postulated.

The vents of the Soufrière-Guadeloupe, Te Maari-Tongariro and Ontake eruptions were also described as elongated fractures (consistent with our findings from the numerical modelling) accounting for the directionality of the PDCs (Sheridan et al. 1980; Lube et al. 2014; Oikawa et al. 2016). However, in nature, further complexity can be observed in both the spatial and temporal evolution of a vent system; this was not possible to address in numerical simulations. For example, inclination of the fracture opening would likely enhance directional effects and fallout of ballistic blocks in specific sectors around the volcano. At Te Maari, the westward directed blast was produced by a series of explosions with a fragmentation front that migrated from west to east. As the lava was fragmented, producing a large number of ballistic blocks, the fragmentation front migrated eastward and different lithologies were involved; the ejection direction also changed, producing a different distribution of the ballistics with time (Breard et al. 2014; Fitzgerald et al. 2014; Montanaro et al. 2016a).

Regarding the explosive mechanism, the Bandai and Te Maari-Tongariro events were triggered and laterally directed by a combination of sudden depressurisation of the hydrothermal system due to a landslide, and lateral and localised vent opening (Yamamoto et al. 1999; Breard et al. 2014, 2015). Additional complexity was observed at Te Maari, where potential fluid injection occurred weeks prior to the eruption (Jolly et al. 2014) and the first blast actually was eastern-directed (in the opposite direction to the landslide), while the second and most powerful blast was directed westward. For the Zao and Soufrière-Guadeloupe eruptions (Fujinawa et al. 2008), an injection of magma at depth was invoked as a triggering mechanism. The Ontake eruption seems to have been triggered by a pressurised reservoir, potentially associated with the arrival of new magma, temperature increase or sudden critical phase change in the hydrothermal system (Kato et al. 2016; Maeno et al. 2016). This latter case possibly best describes the triggering mechanisms that can be invoked for the BdC eruption. In fact, the lack of evidence of a landslide, coupled with the reconstruction of the summit area prior to eruption, suggests that the lavas filling the crater area possibly exacerbated a process of pressure build-up within the hydrothermal system.

Table 4 Comparison between the Breccia di Commenda eruption and other hydrothermal eruptions

	Fossa cone (thirteenth century AD Breccia di Commenda)	Bandai (1888)	Adatara (1900)	Zao (1895)	Soufrière de Guadeloupe (1975–1977)	Te Maari (6 August 2012)	Ontake (27 September 2014)
Dormancy period (years)	?	101	1	4	10	84	7
Trigger	Input of magmatic gas due to deep mafic injection	Depressurisation of the hydrothermal system	Thermal energy of hydrothermal fluids	Shallow intrusion	Input of magmatic gas due dike injection/shallow intrusion	Depressurisation of the hydrothermal system	Depressurisation of the hydrothermal system
Pre-blast phase							
Duration	?	0	1 year	1 year	1 year	1 month	0
	Ash-explosions	No pre-climactic phase	Increase fumaroles discharge; slight quakes; ash explosions	Increase fumaroles discharge; ash explosions	Seismic activity; increase fumaroles discharge; steam explosions, ash explosions	Increased seismic and hydrothermal activity commenced a month before the eruption. Strong increase in late July 2012	A seismic swarm occurred during 6–7 days before but declined over the following days. The frequency of volcano tectonic (VT) earthquakes gradually increased 11 days and peaked on 6 before the eruption
Blast phase							
Duration	?	20 min	7.30 h	?	48 min	6–7 min	3–6 min
Number of events	3 (at least)	More than 20	5 (the last was the most energetic)	1	1	6 events ≈95% of the energy was released during four distinct pulses of explosions within the initial 20 s	3 events lasted 23 min
Directed vs. radial	Initial directed ballistic and radial PDC, then directed PDCs and radial PDC	Directed	Radial	Radial	Directed	Initial directed ballistics and PDCs, then radial PDCs	Three main branches
Maximum travel distance	> 2.2 km	Up to 6 km	Up to 2.4 km	< 0.5 km	3.5 km	2.5 km	Maximum 2.4 km
Area affected by PDCs	Up to 4.6 km^2	13 km^2				6.1 km^2	
Volume of PDC deposits	2.9×10^{-4} km^3	10^{-3} km^3	2.8×10^{-4} km^3	10^{-6} km^3	6×10^{-4} km^3	3.4×10^{-4} km^3	$4–7 \times 10^{-4}$ km^3
Range of ballistic-ejection	Up to 2.2 km	?	?	?	Hundreds of metres	> 2 km (covered area 5.1×10^6 m^2)	
Amount of juvenile material	?	0	0	0	0	0	0

Data from Le Guern et al. (1980); Heiken et al. (1980); Sheridan (1980); Yamamoto et al. (1999); Lube et al. (2014); Breard et al. (2014, 2015); Kato et al. (2016); Maeno et al. (2016)

Simultaneity of the BdC with the Rocche Rosse eruption from Lipari

The simultaneity of the BdC and the Rocche Rosse eruptions suggests that links between the two magmatic systems may exist. The last eruption on the Island of Lipari is thought to have been triggered by the injection of mafic magma into a zoned latitic–rhyolitic magma chamber (Davì et al. 2009b). The absence of a hydrothermal system in the NE part of the Island of Lipari probably favoured the development of a pure magmatic eruption (Davì et al. 2011) with a large dispersal area (Bescoby et al. 2008; Albert et al. 2017; Caron et al. 2012), whereas the presence of a hydrothermal system within the La Fossa cone (Fulignati et al. 1998) favoured the high-energy hydrothermal pulsating eruption of Vulcano. In addition, there is evidence that a strong contribution to the development of a hydrothermal system occurred just towards the end of the Palizzi eruptive unit (Fulignati et al. 2018). Recent observations by Biggs et al. (2016) showed that volcanoes fed by magma bodies that are spaced less than about 10 km apart generally could have simultaneous eruptions, while stress changes can couple large eruptions over distances of about 20–40 km. Simultaneous activation of multiple vents can be particularly relevant in caldera settings (Roggensack et al. 1996; Pistolesi et al. 2016). In the case of the BdC and the Rocche Rosse eruptions (vents located 12 km apart), the magmatic and tectonic links have already been proposed by several authors (Ventura et al. 1999; Gioncada et al. 2003; Ruch et al. 2016), and concurrent eruptions could be facilitated by the occurrence of a stress change (large earthquake) along the Aeolian–Tindari–Letojanni fault zone. A similar coupled event has been recognised at Tarawera volcano and at the nearby Waiotapu geothermal field (New Zealand). This has been attributed to a basaltic intrusion at depth, capable of triggering both a magmatic (the Tarawera rhyolitic) and the hydrothermal (Waiotapu) ~ AD 1315 eruptions from vents situated more than 10 km one from the other (Nairn et al. 2005).

Possible occurrence of a new BdC-like eruption at Vulcano and associated hazards

The data presented here and the comparison with similar eruptions provide important insights into potential future hydrothermal eruptions at the La Fossa cone. The increase and decrease in pressure in the La Fossa cone hydrothermal system are responsible for maintaining high fluid permeability while maintaining existing fractures in the cone (Paonita et al. 2013; Capasso et al. 2014). Therefore, nowadays the low permeability conditions that would have affected the explosion during the BdC eruption are unlikely. However, it cannot be ruled out that the occurrence of landslides during periods of high pressure can trigger a hydrothermal eruption like the Bandai and Te Maari-Tongariro events. In addition, it should be considered that La Fossa cone pressurisation may be one of the causes of flank instability (Reid 2004; Thomas et al. 2004). Considering this, even in the absence of the same predisposing factors of the BdC eruption (low permeability in the summit area), the increase in the amount of gas in the hydrothermal system could promote internal volcano pressurisation that might in turn produce the increase in pore pressure and the consequent flank instability, generating landslide-triggered hydrothermal explosions. In the same way, the possibility that a hydrothermal eruption at La Fossa cone can be triggered by a strong release of gas from the magma chamber following movements of the regional faults that are present in the Vulcano–Lipari area cannot be excluded (Montalto 1995).

If a BdC-like eruption were to happen again at La Fossa, the impact on the island would be catastrophic and far larger than that associated with a Vulcanian-type eruption. In fact, hazards associated with a BdC-like eruption include both dilute and dense PDCs with a possible blast component, intense and long-lasting tephra fallout and highly concentrated sedimentation of ballistic blocks up to 2 km from vent. Modelling of PDCs has in particular indicated a run-out up to 2.3 km in the direction of Piano and more than 3 km towards the NW. Considering the proximity of residential buildings and both critical facilities and infrastructures to La Fossa edifice and the high-to-very-high vulnerability of the associated urban fabrics (Galderisi et al. 2013; Biass et al. 2016a,b), depending on the position and the geometry of the eruptive vent, the resulting impact could affect the Vulcano community and surrounding islands at multiple scales.

In such a scenario, an effort will be needed to identify the possible precursors of hydrothermal eruptions, not only considering the 'classical' geochemical (Chiodini et al. 1995; Capasso et al. 1999; Granieri et al. 2006) and in situ geophysical (Montalto 1995; Fournier and Jolly 2014; Hurst et al. 2014; Honda et al. 2018) monitoring but also considering the opportunities provided by the new and advanced remote sensing techniques (Kobayashi 2018; Kobayashi et al. 2018).

Conclusions

Deposits related to the blast phase of the BdC eruption show close similarities with those recently produced at Te Maari-Tongariro (2012) and Ontake (2014) volcanoes, such as the lithic nature of the components, moderate volume of the emitted products and the strong directionality of the eruptive jets (ballistic blocks and dilute PDCs). Despite the difficulties of comparing the BdC eruption with recent events which were directly observed, the reconstructed eruptive sequence displays similar features, with a laterally directed, fines-depleted blast followed by a final, central vent eruption. Multiple explosions from fissure-like vents have been observed at both the Te Maari-Tongariro and Ontake isolated

hydrothermal blasts and are also necessary to model the phase 2a of BdC. In such a scenario, large ballistic blocks (up to 30 cm in diameter) initially at rest can be accelerated up to 200 m/s by drag and pressure forces eventually producing concentrated showers of blocks to distances larger than 2 km from the vent.

The blast phase of the BdC eruption (phase 2a) was preceded by mild ash emissions (phases 1a and 1b), accounting for a recognisable precursory phase (probably days before the blast). Precursory phases were reported for the eruption of Zao (1895), Adatara (1900) and Soufrière-Guadeloupe (1976), but not for Te Maari-Tongariro and Ontake. Regardless of the existence of predisposing conditions (increased overpressure due to rapid rise of high-pressure gas masses or rapid decompression due to landslides), the increase in the amount of gas in the hydrothermal system is to be considered to be the overall trigger of these eruptions.

The high permeability of the system and the absence of a lava cap at the summit of the cone suggest that the current conditions at La Fossa are not favourable to generate a BdC-like eruption. Nonetheless, the detailed understanding of the alteration style and intensity as well as the spatial distribution of lithology within the very shallow (within metres) part in the cone area (e.g. Heap et al. 2017; Mayer et al. 2016, 2017) would yield essential information in relation to eventual future unrest phases. This information should also be accompanied by geophysical/geochemical parameters (deformation, thermal flux, gas flux time series) that might indicate a decrease of permeability and an augmented pore pressure (e.g. Fournier and Jolly 2014; Honda et al. 2018; Kobayashi et al. 2018).

In addition, two eruptions should also be considered. As an example, the temporal coincidence of the BdC event with the Rocche Rosse rhyolitic eruption 12 km away from the La Fossa cone is closely reminiscent of the contemporaneity of events that occurred at Tarawera and the Waiotapu geothermal vents situated 10 km apart. Such a contemporaneity of magmatic and hydrothermal events possibly indicates that the activation of regional faults could be an important factor facilitating the rise of high-pressure masses of gas through sudden increase of permeability along the fault plane. In this sense, we emphasise the importance of geophysical parameters in indicating an increase or decrease in permeability and/or of seismic activity.

Acknowledgments C. Bonadonna was supported by the Swiss National Science Foundation (subside no. 200021-129997). The authors are grateful to R. Fusillo (Univ. Bristol) for assistance during the fieldwork. F. di Traglia was supported by a post-doctoral fellowship founded by the 'Università degli Studi di Firenze—Ente Cassa di Risparmio di Firenze' (D.R. n. 127804 (1206), 2015). The authors are grateful to the 'INGV-Sezione di Palermo' staff, especially to P. Madonia, for the logistic support at the 'M. Carapezza' Volcanological Observatory (Island of Vulcano) during field activities. L. Gurioli and C. Montanaro are acknowledged for their careful and constructive reviews which greatly enhanced the quality of the manuscript, and Pierre-Simon Ross for editorial handling.

Eulerian–Eulerian model for the gas–pyroclasts mixture

The Eulerian–Eulerian multiphase flow model formulation has been modified from Neri et al. (2003) for one single particulate class, representing fine ash. For the two-phase gas–particle mixture, the following transport equations for mass, momentum and energy are solved. All symbols and units are defined in Appendix 4.

Mass equations

$$\frac{\partial\left(\alpha_g\rho_g\right)}{\partial t}+\nabla\cdot\left(\alpha_g\rho_g\mathbf{U}_g\right)=0$$
$$\frac{\partial(\alpha_s\rho_s)}{\partial t}+\nabla\cdot(\alpha_s\rho_s\mathbf{U}_s)=0$$

Momentum equations

Because particle–particle collisions are neglected (see below), only the gas pressure term is included in the particle momentum equation (Gidaspow's Model A, 1994).

$$\frac{\partial}{\partial t}\left[\alpha_g\rho_g\mathbf{U}_g\right]+\nabla\cdot\left[\alpha_g\rho_g\mathbf{U}_g\mathbf{U}_g\right]==-\alpha_g\nabla P-\nabla\cdot\left(\alpha_g\rho_g\mathbf{T}_g\right)+\alpha_g\rho_g\mathrm{g}+D_{gs}\left(\mathbf{U}_s-\mathbf{U}_g\right)$$
$$\frac{\partial}{\partial t}\left[\alpha_s\rho_s\mathbf{U}_s\right]+\nabla\cdot\left[\alpha_s\rho_s\mathbf{U}_s\mathbf{U}_s\right]==-\alpha_s\nabla P-\nabla\cdot\left(\alpha_s\rho_s\mathbf{T}_s\right)+\alpha_s\rho_s\mathrm{g}-D_{gs}\left(\mathbf{U}_s-\mathbf{U}_g\right)$$

Energy equations

The total energy of the i-th phase is defined as the sum of the specific internal e_i and kinetic k_i energy ($k=\frac{1}{2}\mathbf{U}^2$). The work done by gravity and by the drag force is neglected in both balances. Heat conductivity terms are neglected for particles when focusing on the dilute flow regime.

$$\frac{\partial}{\partial t}\left[\alpha_g\rho_g\left(e_g+k_g\right)\right]+\nabla\cdot\left[\alpha_g\rho_g\left(e_g+k_g\right)\mathbf{U}_g\right]=$$
$$=-\nabla\cdot\left(\alpha_g\mathbf{q}_g\right)-\left[p\frac{\partial\alpha_g}{\partial t}+\nabla\cdot\left(\alpha_g\mathbf{U}_g p\right)\right]+K_{ht}\left(T_s-T_g\right)$$
$$\frac{\partial}{\partial t}\left[\alpha_s\rho_s(e_s+k_s)\right]+\nabla\cdot\left[\alpha_s\rho_s(e_s+k_s)\mathbf{U}_s\right]=$$
$$=-\left[P\frac{\partial\alpha_s}{\partial t}+\nabla\cdot(\alpha_s\mathbf{U}_s P)\right]+K_{ht}\left(T_g-T_s\right)$$

Closure equations

The two phases are treated as interpenetrating continua. Their volume fractions obey the closure equation:

$$\alpha_g+\alpha_s=1$$

The thermal equation of state of the gas phase is that of perfect gases. Particle density is constant.

$$\rho_g = \rho_g(P, T_g)$$
$$\rho_s = \text{constant}$$

The frictional and collisional momentum dissipation terms in the particle stress tensors are neglected because they are negligible in the mixture expansion phase and in the dilute regime of pyroclastic flow propagation (Esposti Ongaro et al. 2016). Although they can be important in the basal layer and in the stopping regime of pyroclastic flow emplacement, we have neglected them to speed computation up. Stress terms have been switched on in a couple of runs to ensure that their effect was negligible on large-scale dynamics. On the contrary, turbulent sub-grid stress terms have always been included. For both the gas and particles, the stress tensor is written in a Newtonian form:

$$\mathbf{T}_\mathrm{i} = -2\mu_\mathrm{eff}\mathbf{S}_\mathrm{i} - \lambda_\mathrm{i}(\nabla\cdot\mathbf{U}_\mathrm{i})\mathbf{I}$$
$$\mathbf{S}_\mathrm{i} = \frac{1}{2}\left(\nabla\mathbf{U}_\mathrm{i} + \nabla\mathbf{U}_\mathrm{i}^\mathrm{T}\right) - \frac{1}{3}(\nabla\cdot\mathbf{U}_\mathrm{i})\mathbf{I}$$

where the subscript (i) indicates either gas or particles and ν_eff is the effective viscosity coefficient ($\mu_\mathrm{eff} = \mu + \mu_\mathrm{turb}$), and is the sum of the molecular/granular viscosity μ (equal to 1.84×10^5 Pa s, for gas, and to zero for particles) and the turbulent (subgrid) turbulent coefficient.

The heat flux is expressed through Fourier's law, for both gas and particles:

$$\mathbf{q}_\mathrm{i} = -\rho_i\left(D_i + \frac{\nu_\mathrm{turb}}{Pr}\right)\frac{C_{P,i}}{C_{V,i}}\nabla e_\mathrm{i}$$

where Pr is the turbulent Prandtl number, set equal to 0.7 for gas and 1 for particles and $\nu_\mathrm{turb} = \mu_\mathrm{turb}/\rho_\mathrm{i}$.

Finally, the gas–particle drag coefficient D_{gs} is expressed by the Ergun–Wen–Yu law, whereas the gas–particle heat transfer coefficient K_{ht} is expressed by the Ranz–Marshall law. We refer to Neri et al. (2003) for such details.

The Eulerian–Eulerian model is solved by means of a segregated, semi-implicit solution algorithm implemented in the twoPhaseEulerFoam application of OpenFOAM (www.openfoam.org, version 4.1). The original solver has been modified by the authors to account for atmospheric vertical stratification.

Lagrangian model for ballistics

The numerical solver adopted in this work is based on a Lagrangian approach for the larger clasts (de' Michieli Vitturi et al. 2010; Del Bello et al. 2017), using the `KinematicCloud` class implemented in OpenFOAM. In the present application, the Lagrangian trajectories are calculated by imposing a one-way coupling with the continuous phases (gas and fine particles), i.e. Lagrangian particles are influenced by the fluid field but their mass fraction is low enough to neglect their influence on the fluid.

In the Lagrangian formulation, trajectories are obtained by integrating, for each particle P with mass m_p and velocity $\mathbf{U}_p$, the Newton equation of motion expressing acceleration of a particle as a function of the sum of the forces acting on the particle:

$$m_p\frac{\mathrm{d}\mathbf{U}_p}{\mathrm{d}t} = \sum\mathbf{F}_p$$

In this application, we considered the steady state fluid-particle drag $\mathbf{F}_\mathrm{D}$, the pressure gradient $\mathbf{F}_\mathrm{G}$ and the body force $\mathbf{F}_\mathrm{B}$ (i.e. gravity). Virtual mass, Magnus and Basset forces are neglected as their magnitude is usually much smaller (de' Michieli Vitturi et al. 2010):

$$\sum\mathbf{F}_p = \mathbf{F}_D + \mathbf{F}_P + \mathbf{F}_G$$

In dilute flows, such as those of interest in this work, the dominant force acting on the particles (besides gravity $\mathbf{F}_\mathrm{G} = m_P\mathbf{g}$) is the drag exerted by the fluid phase, expressed by:

$$\mathbf{F}_D = \frac{1}{2}\rho_C|\mathbf{U}_C - \mathbf{U}_P|(\mathbf{U}_C - \mathbf{U}_P)C_D\pi\left(\frac{D_P}{2}\right)^2$$

In this expression, D_P is the particle diameter, whereas the subscripts C and P indicate the continuous phase and the particle, respectively. For the drag coefficient C_D, we adopt the same expression used by Neri et al. (2003):

$$C_D = \frac{24}{Re}\left(1 + 0.15\,Re^{0.687}\right)$$

valid up to $Re = 1000$, with the particle Reynolds number Re defined as:

$$Re = \frac{\rho_C|\mathbf{U}_C - \mathbf{U}_P|D_P}{\mu_C}$$

where ρ_C is the density of the carrier phase, $\mathbf{U}_\mathrm{C}$ is its velocity and μ_C is the dynamic viscosity.

De' Michieli Vitturi et al. (2010) already demonstrated that, in the initial stages of a Vulcanian eruption, the pressure gradient terms are of the same order of magnitude as the drag term. In our work, we thus included the pressure gradient in the Lagrangian equations and noticed that this term is a fundamental one to correctly estimate the ballistic ranges. Neglecting the pressure gradient entails a decrease of the maximum distance reached by 30 cm particles by about 25% (i.e. from 1.90 to 1.45 km).

The pressure gradient force is written as:

$$\mathbf{F}_G = -\frac{m_P}{\rho_P}\nabla P$$

All force terms are first computed at the centres of the computational cells and then linearly interpolated at the particle position to update particle velocity. Finally, new particle positions are obtained by integration of the velocity:

$$\frac{d\mathbf{x}_p}{dt} = \mathbf{U}_p$$

Topographic boundary conditions and numerical mesh

The Digital Elevation Model (DEM) represents the present topography of the Vulcano island, with the crater filled up to the rim (Fig. C1a). At time $t = 0$, the eruptive mixture is confined within a shallow fissure excavated in the crater area. To reproduce the observed spreading in East-Southeast directions, the fissure was oriented N35°E, the inner profile was asymmetrically opened towards Southeast (Fig. C1b) and ballistic particles where located along the southeastern margin of the fissure. It is worth remarking that asymmetric ballistic launch can be produced in natural systems by an oriented fissure or an inclined jet but, in our application, it was not possible to test such a geometry. In any case, our study demonstrates that ballistic particles ejected towards the East-Southeast can reach, with the selected initial conditions, the observed ranges.

The DEM was converted in STL format and the computational grid was adapted to the topography by using the snappyHexMesh utility, implemented in OpenFOAM 4.1. The computational domain is extended 4.6 km in the x direction (West-East), 4.3 km in the y direction (South-North) and 2.5 km vertically. An initial coarse, rectilinear uniform mesh (with 100 m resolution in all directions) was refined in two steps, to obtain a 25-m resolution at the ground surface. Two terrain-following layers were then added, with an average vertical resolution of 10 m. Such a local refinement allowed to have enough resolution to resolve the large-scale features of dilute and thick pyroclastic density currents (Esposti Ongaro et al. 2016), while keeping affordable the number of computational cells (~ 280,000) and the simulation time (~ 3 h) for simulation on a Intel i5 4-cores (3.2 GHz) PC.

List of mathematical symbols

Symbols	Meaning	Dimensions
α	Volume fraction	
ρ	Density	$[kg][m]^{-3}$
$\mathbf{U}$	Velocity	$[m][s]^{-1}$
P	Pressure	$[Pa] = [kg][m]^{-1}[s]^{-2}$
T	Temperature	[K]
e	Specific thermal energy	$[J][kg]^{-1} = [m]^2[s]^{-2}$
k	Specific kinetic energy	$[m]^2[s]^{-2}$
$\mathbf{T}$	Stress tensor	[Pa]
$\mathbf{q}$	Energy flux	$[kg][s]^{-3}$
$\mathbf{S}$	Deviatoric tensor	$[s]^{-1}$
g	Gravity acceleration	$[m][s]^{-2}$
D_{gs}	Gas–particle drag coefficient	$[kg][m]^{-3}[s]^{-1}$
K_{ht}	Gas–particle heat exchange coefficient	$[kg][m]^{-1}[s]^{-3}[K]^{-1}$
ν	Kinematic viscosity coefficient	$[m]^2[s]^{-1}$
μ	Dynamic viscosity coefficient	[Pa][s]
λ	Secondary dynamic viscosity coefficient	[Pa][s]
D_i	Heat diffusion coefficient for phase i	$[m]^2[s]^{-1}$
$C_{P,i}$	Specific heat at constant pressure for phase i	$[J][kg]^{-1}[K]^{-1}$
$C_{V,i}$	Specific heat at constant volume for phase i	$[J][kg]^{-1}[K]^{-1}$
R	Specific gas constant	$[J][kg]^{-1}[K]^{-1}$
n	Gas mass fraction	
ϕ	Porosity (gas volume fraction) of the exploding mixture	
m_p	Ballistic particle mass	[kg]
$\mathbf{F}$	Force acting on a ballistic particle	$[kg][m][s]^{-2}$
Re	Reynolds number	
Pr	Prandtl number	
Subscripts		
g	Gas phase	
s	Solid particulate phase	

References

Albert PG, Tomlinson EL, Smith VC, Di Traglia F, Pistolesi M, Morris A, Donato P, De Rosa R, Sulpizio R, Keller J, Rosi M (2017) Glass geochemistry of pyroclastic deposits from the Aeolian Islands in the last 50 ka: a proximal database for tephrochronology. J Volcanol Geotherm Res 336:81–107

Arrighi S, Tanguy JC, Rosi M (2006) Eruptions of the last 2200 years at Vulcano and Vulcanello (Aeolian Islands, Italy) dated by high-accuracy archeomagnetism. Phys Earth Planet Int 159:225–233

Barde-Cabusson S, Finizola A, Revil A, Ricci T, Piscitelli S, Rizzo E, Angeletti B, Balasco M, Bennati L, Byrdina S, Carzaniga N, Crespy A, Di Gangi F, Morin J, Perrone A, Rossi M, Roulleau E, Suski B, Villeneuve N (2009) New geological insights and structural control on fluid circulation in La Fossa cone (Vulcano, Aeolian Islands, Italy). Journal of volcanology and Geothermal Research, 185(3): 231–245

Barberi F, Bertagnini A, Landi P, Principe C (1992) A review on phreatic eruptions and their precursors. J Volcanol Geotherm Res 52:231–246

Belousov A (1996) Deposits of the 30 march 1956 directed blast at Bezymianny volcano, Kamchatka, Russia. Bull Volcanol 57(8): 649–662

Belousov A, Voight B, Belousova M (2007) Directed blasts and blast-generated pyroclastic density currents: a comparison of the Bezymianny 1956, mount St Helens 1980, and Soufrière Hills, Montserrat 1997 eruptions and deposits. Bull Volcanol 69:701

Bescoby D, Barclay J, Andrews J (2008) Saints and sinners: a tephrochronology for late antique landscape change in Epirus from the eruptive history of Lipari, Aeolian Islands. J Archeol Sci 35: 2574–2579

Biass S, Bonadonna C, Di Traglia F, Pistolesi M, Rosi M, Lestuzzi P (2016a) Probabilistic evaluation of the physical impact of future tephra fallout events for the island of Vulcano, Italy. Bull Volcanol 78:1–22

Biass S, Falcone JL, Bonadonna C, Di Traglia F, Pistolesi M, Rosi M, Lestuzzi P (2016b) Great balls of fire: a probabilistic approach to quantify the hazard related to ballistics—a case study at La Fossa volcano, Vulcano Island, Italy. J Volcanol Geotherm Res 325:1–14

Biggs J, Robertson E, Cashman K (2016) The lateral extent of volcanic interactions during unrest and eruption. Nat Geosci 9(4):308

Bonadonna C, Costa A (2012) Estimating the volume of tephra deposits: a new simple strategy. Geology 40:415–418

Boudon G, Lajoie J (1989) The 1902 Peléean deposits in the fort cemetery of St. Pierre, Martinique: a model for the accumulation of turbulent nuees ardentes. In: G Boudon and A Gourgaud (Editors), Mount Pelée J Volcanol Geotherm Res 38:113–130

Breard ECP, Lube G, Cronin SJ, Fitzgerald R, Kennedy B, Scheu B, Montanaro C, White JDL, Tost M, Procter JN, Moebis A (2014) Using the spatial distribution and lithology of ballistic blocks to interpret eruption sequence and dynamics: august 6 2012 upper Te Maari eruption, New Zealand. J Volcanol Geotherm Res 286:373–386

Breard ECP, Lube G, Cronin SJ, Valentine GA (2015) Transport and deposition processes of the hydrothermal blast of the 6 august 2012 Te Maari eruption, Mt. Tongariro. Bull Volcanol 77:100

Brissette FP, Lajoie J (1990) Depositional mechanics of turbulent nuees ardentes (surges) from their grain sizes. Bull Volcanol 53:60–66

Browne P, Lawless J (2001) Characteristics of hydrothermal eruptions, with examples from New Zealand and elsewhere. Earth Sci Rev 52: 299–331

Bullock LA, Gertisser R, O'driscoll B (2018) Emplacement of the Rocche Rosse rhyolite lava flow (Lipari, Aeolian Islands). Bull Volcanol 80(5):48

Burns FA, Bonadonna C, Pioli L, Cole PD, Stinton A (2017) Ash aggregation during the 11 February 2010 partial dome collapse of the Soufrière Hills volcano, Montserrat. J Volcanol Geotherm Res 335:92–112

Calvache VML, Williams SN (1992) Lithic-dominated pyroclastic flows at Galeras volcano, Colombia—an unrecognised volcanic hazard. Geology 20:539–542

Capaccioni B, Coniglio S (1995) Varicolored and vesiculated tuffs from La Fossa volcano, Vulcano Island (Aeolian archipelago, Italy): evidence of syndepositional alteration processes. Bull Volcanol 57:61–70

Capasso G, Favara R, Inguaggiato S (1997) Chemical features and isotopic composition of gaseous manifestations on Vulcano Island, Aeolian Islands, Italy: an interpretative model of fluid circulation. Geochim Cosmochim Acta 61(16):3425–3440

Capasso, G., Favara, R., Francofonte, S., Inguaggiato, S. (1999). Chemical and isotopic variations in fumarolic discharge and thermal waters at Vulcano Island (Aeolian Islands, Italy) during 1996: evidence of resumed volcanic activity. Journal of Volcanology and Geothermal Research, 88(3), 167–175.

Capasso G, Federico C, Madonia P, Paonita A (2014) Response of the shallow aquifer of the volcano-hydrothermal system during the recent crises at Vulcano Island (Aeolian archipelago, Italy). J Volcanol Geotherm Res 273:70–80

Caron B, Siani G, Sulpizio R, Zanchetta G, Paterne M, Santacroce R, Tema E, Zanella E (2012) Late Pleistocene to Holocene tephrostratigraphic record from the northern Ionian Sea. Mar Geol 311-314:41–51

Carn SA, Watts RB, Thompson G, Norton GE (2004) Anatomy of a lava dome collapse: the 20 March 2000 event at Soufrière Hills volcano, Montserrat. J Volcanol Geotherm Res 131:241–264

Cerminara M, Esposti Ongaro T, Berselli LC (2016) ASHEE-1.0: a compressible, equilibrium-Eulerian model for volcanic ash plumes. Geosci Model Dev 9:697–730

Chiodini G, Cioni R, Marini L, Panichi C (1995) Origin of the fumarolic fluids of Vulcano Island, Italy and implications for volcanic surveillance. Bull Volcanol 57(2):99–110

Chiodini G, Frondini F, Raco B (1996) Diffuse emission of CO_2 from the Fossa crater, Vulcano Island (Italy). Bull Volcanol 58(1):41–50

Chretien S, Brousse R (1989) Events preceding the great eruption of 8 May 1902 at Mount Pelée, Martinique. J Volcanol Geotherm Res 38: 67–75

Clarke AB, Neri A, Voight B, Macedonio G, Druitt TH (2002) Computational modelling of the transient dynamics of the august 1997 Vulcanian explosions at Soufriere Hills volcano, Montserrat: influence of initial conduit conditions on near-vent pyroclastic dispersal. Mem-Geol Soc London 21:319–348

Cortese M, Frazzetta G, La Volpe L (1986) Volcanic history of Lipari (Aeolian Islands, Italy) during the last 10,000 years. J Volcanol Geotherm Res 27:117–133

De Astis G, Dellino P, La Volpe L, Lucchi F, Tranne CA (2006) Geological map of the Vulcano Island. Litografia artistica cartografica, Firenze

De Astis G, Lucchi F, Dellino P, La Volpe L, Tranne CA, Frezzotti ML, Peccerillo A (2013) Geology, volcanic history and petrology of Vulcano (central Aeolian archipelago). Geol Soc Lond Mem 37: 281–349

De Fiore O (1922) Vulcano (Isole Eolie). In: Friedlaender, I. (Ed.), Rivista Vulcanologica (Suppl. 3): 1–393

de' Michieli Vitturi M, Neri A, Esposti Ongaro T, Lo Savio S, Boschi E (2010) Lagrangian modeling of large volcanic particles: application to Vulcanian explosions. J Geophys Res SE 115(B8)

Dade B, Huppert H (1998) Long-runout rockfalls. Geol 26:803–806

Davì M, De Rosa R, Donato P, Vetere F, Barca D, Cavallo A (2009a) Magmatic evolution and plumbing system of ring-fault volcanism:

the Vulcanello peninsula (Aeolian Islands, Italy). Eur J Mineral 21: 1009–1028

Davì M, De Rosa R, Barca D (2009b) A LA-ICP-MS study of minerals in the Rocche Rosse magmatic enclaves: evidence of a mafic input triggering the latest silicic eruption of Lipari Island (Aeolian arc, Italy). J Volcanol Geotherm Res 182:45–56

Davì M, De Rosa R, Donato P, Sulpizio R (2011) The Lami pyroclastic succession (Lipari, Aeolian Islands): a clue for unravelling the eruptive dynamics of the Monte Pilato rhyolitic pumice cone. J Volcanol Geotherm Res 201:285–300

Del Bello E, Taddeucci J, de' Michieli Vitturi M, Scarlato P, Andronico D, Scollo S, Kueppers U, Ricci T (2017) Effect of particle volume fraction on the settling velocity of volcanic ash particles: insights from joint experimental and numerical simulations. Sci Rep 7:39620

Dellino P, La Volpe L (1995) Fragmentation versus transportation mechanisms in the pyroclastic sequence of Monte Pilato–Rocche Rosse (Lipari, Italy). J Volcanol Geotherm Res 64:211–231

Dellino P, De Astis G, La Volpe L, Mele D, Sulpizio R (2011) Quantitative hazard assessment of phreatomagmatic eruptions at Vulcano (Aeolian Islands, southern Italy), as obtained by combining stratigraphy, event statistics and physical modelling. J Volcanol Geotherm Res 201:364–384

Di Traglia F, Pistolesi M, Rosi M, Bonadonna C, Fusillo R, Roverato M (2013) Growth and erosion: volcanic geology and morphological evolution during the last 1000 years of La Fossa (island of Vulcano, southern Italy). Geomorph 194:94–107

Diliberto IS (2017) Long-term monitoring on a closed-conduit volcano: a 25 year long time-series of temperatures recorded at La Fossa cone (Vulcano Island, Italy), ranging from 250°C to 520°C. J Volcanol Geotherm Res 346:151–160

Erfurt-Cooper P (2011) Geotourism in volcanic and geothermal environments: playing with fire? Geoheritage 3(3):187–193

Esposti Ongaro T, Clarke AB, Voight B, Neri A, Widiwijayanti C (2012) Multiphase flow dynamics of pyroclastic density currents during the May 18, 1980 lateral blast of Mount St. Helens. J Geophys Res SE 117(B6)

Esposti Ongaro T, Orsucci S, Cornolti F (2016) A fast, calibrated model for pyroclastic density currents kinematics and hazard. J Volcanol Geoth Res 327:257–272

Federico C, Capasso G, Paonita A, Favara R (2010) Effects of steam-heating processes on a stratified volcanic aquifer: stable isotopes and dissolved gases in thermal waters of Vulcano Island (Aeolian archipelago). J Volcanol Geotherm Res 192:178–190

Fitzgerald RH, Tsunematsu K, Kennedy BM, Breard ECP, Lube G, Wilson TM, Jolly AD, Pawson J, Rosenberg MD, Cronin SJ (2014) The application of a calibrated 3D ballistic trajectory model to ballistic hazard assessments at upper Te Maari, Tongariro. J Volcanol Geoth Res 286:248–262

Fitzgerald RH, Kennedy BM, Wilson TM, Leonard GS, Tsunematsu K, Keys H (2017) The communication and risk management of volcanic ballistic hazards. Springer, Berlin Heidelberg, pp 1–27

Forni F, Lucchi F, Peccerillo A, Tranne CA, Rossi PL, Frezzotti ML (2013) Stratigraphy and geological evolution of the Lipari volcanic complex (central Aeolian archipelago). Geol Soc London Mem 37: 213–279

Fournier N, Jolly AD (2014) Detecting complex eruption sequence and directionality from high-rate geodetic observations: the August 6, 2012 Te Maari eruption, Tongariro, New Zealand. J Volcanol Geoth Res 286:387–396

Frazzetta G, La Volpe L, Sheridan MF (1983) Evolution of the La Fossa cone, Vulcano. J Volcanol Geotherm Res 17:329–360

Frazzetta G, Gillot PY, La Volpe L, Sheridan MF (1984) Volcanic hazards at La Fossa of Vulcano: data from the last 6000 years. Bull Volcanol 47:105–124

Fujinawa A, Ban M, Ohba T, Kontani K, Miura K (2008) Characterization of low-temperature pyroclastic surges that occurred in the northeastern Japan arc during the late 19th century. J Volcanol Geotherm Res 178:113–130

Fulignati P, Gioncada A, Sbrana A (1998) Geologic model of the magmatic-hydrothermal system of Vulcano (Aeolian Island, Italy). Mineral Petrol 62:195–222

Fulignati P, Gioncada A, Costa S, Di Genova D, Di Traglia F, Pistolesi M (2018) Magmatic sulfide immiscibility at an active magmatic-hydrothermal system: the case of La Fossa (Vulcano, Italy). Volcanol Geotherm Res 358:45–75

Fusillo R, Di Traglia F, Gioncada A, Pistolesi M, Wallace PJ, Rosi M (2015) Deciphering post-caldera volcanism: insight into the Vulcanello (island of Vulcano, southern Italy) eruptive activity based on geological and petrological constraints. Bull Volcanol 77: 76

Galderisi A, Bonadonna C, Delmonaco G, Ferrara FF, Menoni S, Ceudech A, Biass S, Frischknecht C, Manzella I, Minucci G, Gregg C (2013) Vulnerability assessment and risk mitigation: the case of Vulcano Island, Italy, Landslide science and practice, volume 7: social and economic impact and policies. Springer Berlin Heidelberg 55–64

Gardner CA, White RA (2002) Seismicity, gas emission and deformation from 18 July to 25 September 1995 during the initial phreatic phase of the eruption of Soufriere Hills Volcano, Montserrat. In: Druitt, T.H., Kokelaar, B.P. (Eds.), The eruption of Soufriere Hills Volcano, Montserrat from 1995 to 1999. Geol Soc London Mem 21:567–581

Germanovich LN, Lowell RP (1995) The mechanism of phreatic eruptions. J Geophys Res 100:8417–8434

Gidaspow D (1994) Multiphase flow and fluidization: continuum and kinetic theory descriptions. Academic press

Gioncada A, Sbrana A (1991) La Fossa caldera. Vulcano: inferences from deep drillings. Acta Vulcanol 1:115–125

Gioncada A, Mazzuoli R, Bisson M, Pareschi MT (2003) Petrology of volcanic products younger than 42 ka on the Lipari–Vulcano complex (Aeolian Islands, Italy): an example of volcanism controlled by tectonics. J Volcanol Geotherm Res 122:191–220

Granieri D, Carapezza ML, Chiodini G, Avino R, Caliro S, Ranaldi M, Ricci T, Tarchini L (2006) Correlated increase in CO_2 fumarolic content and diffuse emission from La Fossa crater (Vulcano, Italy): evidence of volcanic unrest or increasing gas release from a stationary deep magma body? Geophys Res Lett 33(13)

Gurioli L, Zanella E, Gioncada A, Sbrana A (2012) The historic magmatic–hydrothermal eruption of the breccia di Commenda, Vulcano, Italy. Bull Volcanol 74:1235–1254

Harris AJ, Stevenson DS (1997) Thermal observations of degassing open conduits and fumaroles at Stromboli and Vulcano using remotely sensed data. J Volcanol Geoth Res 76(3–4):175–198

Hincks TK, Komorowski J-C, Sparks SR, Aspinall WP (2014) Retrospective analysis of uncertain eruption precursors at La Soufrière volcano, Guadeloupe, 1975–77: volcanic hazard assessment using a Bayesian belief network approach. J Appl Volcanol 3:3

Hayashi JN, Self S (1992) A comparison of pyroclastic flow and debris avalanche mobility. J Geophys Res Solid Earth 97(B6):9063–9071

Heap MJ, Kennedy BM, Farquharson JI, Ashworth J, Mayer K, Letham-Brake M, Reuschlé T, Albert Gilg H, Scheu B, Lavallée Y, Siratovich P, Cole J, Jolly AD, Baud P, Dingwell DB (2017) A multidisciplinary approach to quantify the permeability of the Whakaari/White Island volcanic hydrothermal system (Taupo volcanic zone, New Zealand). J Volcanol Geoth Res 332:88–108

Heggie TW (2009) Geotourism and volcanoes: health hazards facing tourists at volcanic and geothermal destinations. Travel Med Infect Dis 7(5):257–261

Heiken G, Crowe B, McGetchin T, West F, Eichelberger J, Bartram D, Peterson R, Wohletz K (1980) Phreatic eruption clouds: the activity of la Soufriére de Guadeloupe, F.W.I., August–October. Bull Volcanol 43:383–395

Hoblitt RP (2000) Was the 18 May 1980 lateral blast at Mt St Helens the product of two explosions? Phil Trans R Soc London 358:1639–1661

Honda R, Yukutake Y, Morita Y, Sakai SI, Itadera K, Kokubo K (2018) Precursory tilt changes associated with a phreatic eruption of the Hakone volcano and the corresponding source model. earth. Planets and Space 70(1):117

Houghton BF, Swanson DA, Carey RJ, Rausch J, Sutton AJ (2011) Pigeonholing pyroclasts: insights from the 19 March 2008 explosive eruption of Kīlauea volcano. Geology 39:263–266

Hurst T, Jolly AD, Sherburn S (2014) Precursory characteristics of the seismicity before the 6 August 2012 eruption of Tongariro volcano, North Island, New Zealand. J Volcanol Geotherm Res 286:294–302

Jolly AD, Jousset P, Lyons JJ, Carniel R, Fournier N, Fry B, Miller C (2014) Seismo-acoustic evidence for an avalanche driven phreatic eruption through a beheaded hydrothermal system: an example from the 2012 Tongariro eruption. J Volcanol Geotherm Res 286:331–347

Kato A, Terakawa T, Yamanaka Y, Maeda Y, Horikawa S, Matsuhiro K, Okuda T (2016) Preparatory and precursory processes leading up to the 2014 phreatic eruption of mount Ontake, Japan. Earth, Planets and Space 67:111

Keller J (1980) The island of Vulcano. Rend Soc Italian Miner Petrol 36: 369–414

Kobayashi T (2018) Locally distributed ground deformation in an area of potential phreatic eruption, Midagahara volcano, Japan, detected by single-look-based InSAR time series analysis. J Volcanol Geotherm Res 357:213–223

Kobayashi T, Morishita Y, Munekane H (2018) First detection of precursory ground inflation of a small phreatic eruption by InSAR. Earth Planet Sci Lett 491:244–254

Lajoie J, Boudon G, Bourdier JL (1989) Depositional mechanics of the 1902 pyroclastic Nuee Ardente deposits of Mt. Pelee, Martinique. J Volcanol Geotherm Res 38:131–142

Le Guern F, Bernard A, Chevrier RM (1980) Soufriere of Guadeloupe 1976–1977 eruption-mass and energy transfer and volcanic health hazards. Bull Volcanol 43:577–593

Lube G, Breard EC, Cronin SJ, Procter JN, Brenna M, Moebis A, Pardo N, Stewart RB, Jolly A, Fournier N (2014) Dynamics of surges generated by hydrothermal blasts during the 6 august 2012 Te Maari eruption, Mt. Tongariro, New Zealand. J Volcanol Geotherm Res 286:348–366

Maeno F, Nakada S, Oikawa T, Yoshimoto M, Komori J, Ishizuka Y, Takeshita Y, Shimano T, Kaneko T, Nagai M (2016) Reconstruction of a phreatic eruption on 27 September 2014 at Ontake volcano, Central Japan, based on proximal pyroclastic density current and fallout deposits. Earth, Planets and Space 68:1–20

Mandarano M, Paonita A, Martelli M, Viccaro M, Nicotra E, Millar IL (2016) Revealing magma degassing below closed-conduit active volcanoes: geochemical features of volcanic rocks versus fumarolic fluids at Vulcano (Aeolian Islands, Italy). Lithos 248:272–287

Mannen K, Yukutake Y, Kikugawa G, Harada M, Itadera K, Takenaka J (2018) Chronology of the 2015 eruption of Hakone volcano, Japan: geological background, mechanism of volcanic unrest and disaster mitigation measures during the crisis. Earth, Planets and Space 70: 1–26

Mayberry GC, Rose WI, Bluth GJS (2002) Dynamics of volcanic and meteorological clouds produced on 26 December (Boxing Day) 1997 at Soufriere Hills Volcano, Montserrat In: Druitt, TH, Kokelaar, BP (Eds), The Eruption of Soufriere Hills Volcano, Montserrat, from 1995 to 1999Geol Soc London Mem 21:539–555

Mayer K, Scheu B, Montanaro C, Yilmaz TI, Isaia R, Aßbichler D, Dingwell DB (2016) Hydrothermal alteration of surficial rocks at Solfatara (Campi Flegrei): petrophysical properties and implications for phreatic eruption processes. J Volcanol Geotherm Res 320:128–143

Mayer K, Scheu B, Yilmaz TI, Montanaro C, Gilg HA, Rott S, Joseph EP, Dingwell DB (2017) Phreatic activity and hydrothermal alteration in the valley of desolation, Dominica, Lesser Antilles. Bull Volcanol 79(12):82

Marini L, Principe C, Chiodini G, Cioni R, Fytikas M, Marinelli G (1993) Hydrothermal eruptions of Nisyros (Dodecanese, Greece)—past events and present hazard. J Volcanol Geotherm Res 56:71–94

Mastin LG (1995) Thermodynamics of gas and steam-blast eruptions. Bull Volcanol 57(2):85–98

McKibbin R, Smith T, Fullard L (2009) Components and phases: modelling progressive hydrothermal eruptions. ANZIAM J 50:365. https://doi.org/10.1017/S144618110900011X

Mercalli G, Silvestri O (1891) Le eruzioni dell'isola di Vulcano, incominciate il 3 Agosto 1888 e terminate il 22 Marzo 1880. Annali dell'Ufficio Centrale di Meteorologia e Geodinamica 10:1–213

Miura K, Ban M, Ohba T, Fujinawa A (2012) Sequence of the 1895 eruption of the Zao volcano, Tohoku Japan. J Volcanol Geotherm Res 247:139–157

Montalto A (1995) Seismic assessment of phreatic-explosion hazard at 'La Fossa' Volcano (island of Vulcano, Italy). Nat Hazards 11(1): 57–73

Montanaro C, Scheu B, Cronin SJ, Breard EC, Lube G, Dingwell DB (2016a) Experimental estimates of the energy budget of hydrothermal eruptions; application to 2012 upper Te Maari eruption, New Zealand. Earth Planet Sci Lett 452:281–294

Montanaro C, Scheu B, Gudmundsson MT, Vogfjörd K, Reynolds HI, Dürig T, Strehlow K, Rott S, Reuschlé T, Dingwell DB (2016b) Multidisciplinary constraints of hydrothermal explosions based on the 2013 Gengissig lake events, Kverkfjöll volcano, Iceland. Earth Planet Sci Lett 434:308–319

Montanaro C, Scheu B, Mayer K, Orsi G, Moretti R, Isaia R, Dingwell DB (2016c) Experimental investigations on the explosivity of steam-driven eruptions: a case study of Solfatara volcano (Campi Flegrei). J Geophys Res Solid Earth 121:7996–8014

Nairn IA, Hedenquist JW, Villamor P, Berryman KR, Shane PA (2005) The ~AD1315 Tarawera and Waiotapu eruptions, New Zealand: contemporaneous rhyolite and hydrothermal eruptions driven by an arrested basalt dike system? Bull Volcanol 67:186–193

Napoli R, Currenti G (2016) Reconstructing the Vulcano Island evolution from 3D modeling of magnetic signatures. J Volcanol Geother Res 320:40–49

Neri A, Esposti Ongaro T, Macedonio G, Gidaspow D (2003) Multiparticle simulation of collapsing volcanic columns and pyroclastic flow. J Geophys Res SE 108(B4)

Nicotra E, Giuffrida M, Viccaro M, Donato P, D'Oriano C, Paonita A, De Rosa R (2018) Timescales of pre-eruptive magmatic processes at Vulcano (Aeolian Islands, Italy) during the last 1000 years. Lithos 316-317:347–365

Ohba T, Taniguchi H, Miyamoto T, Hayashi S, Hasenaka T (2007) Mud plumbing system of an isolated phreatic eruption at Akita Yakeyama volcano, northern Honshu, Japan. J Volcanol Geotherm Res 161:35–46

Oikawa T, Yoshimoto M, Nakada S, Maeno F, Komori J, Shimano T, Takeshita Y, Ishizuka Y, Ishimine Y (2016) Reconstruction of the 2014 eruption sequence of Ontake volcano from recorded images and interviews. Earth, Planets and Space 68:79

Paonita A, Federico C, Bonfanti P, Capasso G, Inguaggiato S, Italiano F, Madonia P, Pecoraino G, Sortino F (2013) The episodic and abrupt geochemical changes at La Fossa fumaroles (Vulcano Island, Italy) and related constraints on the dynamics, structure, and compositions of the magmatic system. Geochim Cosmochim Acta 120:158–178

Pardo N, Cronin SJ, Németh K, Brenna M, Schipper CI, Breard E, White JDL, Procter J, Stewart B, Agustín-Flores J, Moebis A, Zernack A, Kereszturi G, Lube G, Auer A, Neall V, Wallace C (2014) Perils in distinguishing phreatic from phreatomagmatic ash; insights into the

eruption mechanisms of the 6 August 2012 Mt. Tongariro eruption, New Zealand. J Volcanol Geotherm Res 286:397–414

Pistolesi M, Isaia R, Marianelli P, Bertagnini A, Fourmentraux C, Albert PG, Tomlinson EL, Menzies MA, Rosi M, Sbrana A (2016) Simultaneous eruptions from multiple vents at Campi Flegrei (Italy) highlight new eruption processes at calderas. Geology 44: 487–490. https://doi.org/10.1130/G37870.1

Pyle DM (1989) The thickness, volume and grainsize of tephra fall deposits. Bull Volcanol 51:1–15

Reid ME (2004) Massive collapse of volcano edifices triggered by hydrothermal pressurization. Geology 32:373–376

Ritchie LJ, Cole PD, Sparks RSJ (2002) Sedimentology of deposits from the pyroclastic density current of 26 December 1997 at Soufrière Hills volcano, Montserrat. Geol Soc London Mem 21:435–456

Roggensack K, Williams SN, Schaefer SJ, Parnell RA (1996) Volatiles from the 1994 eruptions of Rabaul: understanding large caldera systems. Science 273:490–493. https://doi.org/10.1126/science.273.5274.490

Romagnoli C, Casalbore D, Chiocci FL (2012) La Fossa caldera breaching and submarine erosion (Vulcano island, Italy). Mar Geol 303:87–98

Ruch J, Vezzoli L, De Rosa R, Di Lorenzo R, Acocella V (2016) Magmatic control along a strike-slip volcanic arc: the central Aeolian arc (Italy). Tectonics 35:407–424

Sheridan MF (1980) Pyroclastic block flow from the September, 1976, eruption of La Soufrière volcano, Guadeloupe. Bull Volcanol 43: 397–402

Sheridan MF, Malin MC (1983) Application of computer-assisted mapping to volcanic hazard evaluation of surge eruptions: Vulcano, Lipari, and Vesuvius. J Volcanol Geotherm Res 17(1–4):187–202

Soligo M, De Astis G, Delitala MC, La Volpe L, Taddeucci A, Tuccimei P (2000) Uranium-series disequilibria in the products from Vulcano Island (Sicily, Italy): isotopic chronology and magmatological implications. Acta Vulcanol 12:49–59

Stix J, de Moor JM (2018) Understanding and forecasting phreatic eruptions driven by magmatic degassing. Earth. Planets and Space 70(1):83

Strehlow K, Sandri L, Gottsmann JH, Kilgour G, Rust AC, Tonini R (2017) Phreatic eruptions at crater lakes: occurrence statistics and probabilistic hazard forecast. J Appl Volcanol 6:4

Tanaka R, Hashimoto T, Matsushima N, Ishido T (2018) Contention between supply of hydrothermal fluid and conduit obstruction: inferences from numerical simulations. Earth. Planets and Space 70(1):72

Thomas ME, Petford N, Bromhead EN (2004) The effect of internal gas pressurization on volcanic edifice stability: evolution towards a critical state. Terra Nova 16:312–317

Tsunematsu K, Ishimine Y, Kaneko T, Yoshimoto M, Fujii T, Yamaoka K (2016) Estimation of ballistic block landing energy during 2014 mount Ontake eruption. Earth, Planets and Space 68:88

Ventura G (1994) Tectonics, structural evolution and caldera formation on Vulcano Island (Aeolian archipelago, southern Tyrrhenian Sea). J Volcanol Geotherm Res 60(3–4):207–224

Ventura G, Vilardo G, Milano G, Pino NA (1999) Relationships among crustal structure, volcanism and strike–slip tectonics in the Lipari–Vulcano volcanic complex (Aeolian Islands, southern Tyrrhenian Sea, Italy). Phy Earth Plan Int 116(1–4):31–52

Voltaggio M, Barbieri M, Branca M, Castorina F, Taddeucci A, Tecce F, Tuccimei P, Turi B, Vesica P (1997) Calcite in fractures in a volcanic environment (Vulcano Island, Italy): contribution of geochronological and isotopic studies to volcanotectonics. J Volcanol Geotherm Res 75(3–4):271–282

Walker GP (1971) Grain-size characteristics of pyroclastic deposits. J Geol 79:696–714

Woods AW, Sparks RSJ, Ritchie LJ, Batey J, Gladstone C, Bursik MI (2002) The explosive decompression of a pressurized volcanic dome: the 26 December 1997 collapse and explosion of Soufrière Hills volcano, Montserrat. Geol Soc London Mem 21:457–465

Yamamoto T, Nakamura Y, Glicken H (1999) Pyroclastic density current from the 1888 phreatic eruption of Bandai volcano, NE Japan. J Volcanol Geotherm Res 90:191–207